*NRSC-DPA-DPSG-PSDD-JUL 2021-TR-0001877-V1.0*

# Algorithm Theoretical Basis Document: Realization of Surface Reflectance Products from Resourcesat-2/2A: L-3 and AWiFS sensors

**NRSC**

**National Remote Sensing Centre**

**Indian Space Research Organisation**

**Hyderabad-500 037**

**Jul-2021**

# DOCUMENT CONTROL SHEET

| | | | | | |
|---|---|---|---|---|---|
| 1. | **Security classification** | Restricted | | | |
| 2. | **Distribution** | Within ISRO/DOS | | | |
| 3. | **Document (a) Issue:** | **01** | **(b) Revision:** | - | |
| 4. | **Report Type** | Technical | | | |
| 5. | **Report No** | **NRSC-DPA-DPSG-PSDD-JUL 2021-TR-0001877-V1.0** | | | |
| 6. | **Title** | Algorithm Theoretical Basis Document: Realization of Surface Reflectance Products from of Resourcesat-2/2A L-3 and AWiFS sensors. | | | |
| 7. | **Collation** | **Pages** 49 | **Figures** 37 | **Tables** 10 | **References** 15 |
| 8. | **Project** | Land Geophysical Products from IRS Missions | | | |
| 9. | **Author(s)** | V. Keerthi, M. Suresh Kumar,T.Radhika and RN Anjani | | | |
| 10. | **Reviewed by** | Manju Sarma, GD (DPSG) | | | |
| 11. | **Approved by** | Vinod M Bothale, AD (NRSC) | | | |
| 12. | **Affiliation of authors** | NRSC, ISRO | | | |
| 13. | **Originating unit** | PSDD/ DPSG /DPA / NRSC | | | |
| 14. | **Sponsor(s) Name, Type:** | NRSC, ISRO, Govt. of India | | | |
| 15. | **Date of Project Initiation** | Apr, 2016 | | | |
| 16. | **Date of Publication** | Jul, 2021 | | | |
| 17. | **Abstract** | As in abstract page | | | |

# Abstract

This Algorithm Theoretical Basis Document (ATBD) describes a procedure to generate surface reflectance by carrying out atmospheric correction of spectral radiances measured by LISS-3 and AWiFS sensors onboard RS-2 and 2A satellites. The procedure is based on 6S (Second Simulation of Satellite Signal in the Solar Spectrum) model, which is a widely used operational radiative transfer model. The correction is based on Lambertian assumption and corrects for aerosol and molecular absorption and scattering. The aerosol information comes from MODIS satellite products at a resolution of 0.1° and total columnar water vapour and ozone information comes from MODIS atmospheric products at a resolution of 0.05°. Coefficients that are required for atmospheric correction are derived by the 6S code using the above inputs, which are then used to correct RS-2 /2A imagery on a per pixel basis.

The accuracy of surface reflectance (SR) products was validated with both ground and satellite based measurements. Surface reflectance products correlated well with Landsat8 Operational Land Imager (OLI) surface reflectance (LC8) products with correlation coefficient value greater than 85% for all the four bands of RS2 and greater than 94% for RS2A. Retrieved surface reflectance values were also found to be consistent (with in 10%) with ground based Spectro-radiometer measurements. Intra sensor comparison of surface reflectance values were also carried out to further ensure the accuracy of the derived products.Stability, accuracy and temporal consistency of the algorithm was also tested with various datasets.

The fact that atmospheric correction does matter is illustrated using NDVI as an example.

# Contents

# List of Figures

# List of Tables

# Algorithm Theoretical Basis Document: Realization of Surface Reflectance Products from Resourcesat-2/2A: LISS-3 and AWiFS Sensors

## 1.0 Introduction

The fundamental land surface parameter of interest for any remote sensing based application is surface reflectance products. This is because the retrieval of any biophysical parameter demands for the use of precise surface reflectance products as the input. Moreover surface reflectance products are also necessary to uniformly apply a quantitative remote sensing model or set of classification rules to similarly standardized scenes in different regions or years.

The satellite measurements are strongly affected by molecular and aerosol scattering, and absorption by gases, such as water vapor, ozone, oxygen and aerosols. Molecular scattering and absorption by ozone, oxygen and other gases are relatively easy to correct because of the stable concentration of these constituents in both space and time. The most difficult task is to estimate the distribution of aerosols and water vapor as these are highly dynamic in both space and time.

But the real aim is always to know the surface characteristics of the features being mapped and how do they change with time and how they vary in time scales, or with some processes. Signals recorded from the satellite or airborne platforms in the visible and near infrared region are a combination of surface, atmospheric contributions and sensor errors. Thus, to enable quantitative studies of the earth surface, atmospheric perturbations need to be removed from the observed signal. The process of removing atmospheric contribution is commonly referred as atmospheric correction or atmospheric compensation.

Atmospheric correction of optical remotely sensed data can indeed be categorized into two major classes:

• Relative atmospheric correction based on image processing. This correction is simple to apply and does not require atmospheric data. This method extracts information on atmospheric properties directly from images when ancillary data on atmospheric conditions are not available. The best known and most widely used technique, based on images, is the Dark Object Subtraction (DOS) [1].

• Absolute atmospheric correction. On the other hand, this correction is based on the physical process of Radiative Transfer (RT) and is, therefore, very complex and it requires a great amount of information regarding sun-surface sensor geometry, atmospheric condition at the time of data acquisition, and radiometric specifications of the sensor.

The relative methods are computationally fast, but may not work on all images and information pertaining to the atmosphere is not derived in these approaches. These techniques are considered more of a calibration tool than an atmospheric correction model.

Radiative Transfer is the physical phenomena of electromagnetic radiation propagation through a medium. The equation of radiative transfer describes mathematically all sorts of interactions (absorption, emission and scattering). Analytic solutions to the Radiative Transfer Equation (RTE) exist for simple cases [2] but, for a more realistic medium, implying complex multiple scattering effects, numerical methods are required. Radiative Transfer Codes (RTC) are developed to solve the RTE inverting differential equations, in general these models are capable of performing computation over any kind of ”radiance-medium interactions” problem. Several Radiative Transfer codes are available, developed for analysis of atmospheric interactions in particular ranges of the electromagnetic spectrum. Usually RTCs are created on purpose for specific applications. The most known are the Line-By-Line Radiative Transfer Model (LBLRTM) based on the Fast Atmospheric Signature CODE (FASCODE) [3], Spherical HARMonics (SHARM) [4],Radiative Transfer 3 (RT3) [5], the MODerate resolution TRANsmittance code and the Second Simulation of the Satellite Signal in the Solar Spectrum (6S) [6]. All codes listed above solve Transfer Equation in the scalar form, except 6S which can solve it in both scalar and vector form. This means that 6S in vector mode is capable of taking into account the light polarization contributions. Recent studies have shown that neglecting this effect could lead to an error up to 10% between simulated and measured radiance [7-9]. The most widely used models in Remote Sensing for Atmospheric correction on airborne or space-borne images are currently MODTRAN (now available in its 4th release) and 6S. This is due to their capability and adaptability in modelling atmosphere for a wide range of wavelengths and for several different atmospheric boundary conditions.

There are also several commercial packages for atmospheric corrections, among others, Fast Line-of-sight Atmospheric Analysis of Spectral Hypercube (FLAASH) model and Atmospheric Topographic Correction (ATCOR) model are very popular. Both models are based on MODTRAN-4. Atmospheric correction using FLAASH and ATCOR provides comparable accuracy [1-3] w.r.t6S but these modules cannot be used freely because it is licensed. The 6S model is widely used today because it has very good accuracy, freely downloadable and can be run online.

**Hence 6S based atmospheric correction method to realize surface reflectance from RS2/2A sensors was chosen.**

Atmospheric correction is normally performed in two stages. In the first step, the atmospheric properties are determined at the time of satellite overpass. Secondly, a radiative transfer model of the atmosphere is inverted to estimate surface reflectance, accounting for the atmospheric scattering and absorption.

We have developed fully automated atmospheric correction procedure to generate surface reflectance products from RS2 AWiFS and LISS-3 digital data using the 6S (Second Simulation of the Satellite Signal in the Solar Spectrum) radiative transfer model. This procedure employs MODIS atmospheric data products to arrive at the surface reflectance products. Atmospheric input parameters derived from these products include atmospheric water vapour, aerosol optical depth at 550nm (AOD) and ozone. The atmospheric correction tool can generate the correction coefficients based on adaptive grid, using which surface reflectance is derived on a per pixel basis. The atmospherically corrected surface reflectance values derived using the Lambertian approximation.

The following section gives a brief description of the algorithm and methodology that is adopted to arrive at these products. The validation results using near simultaneous, ground and satellite measurements are presented in Section 3. In Section 4 effect of atmospheric correction on NDVI is presented as an application example. A brief summary is given in section 5.

# 2.0 Algorithm and Methodology

## 2.1 Algorithm Description

The atmospheric “perturbation” of a surface reflectance signal depends on the type and characteristics of atmospheric particles interacting with incident solar radiation. Different gas molecules ($N_2$, $O_2$, $O_3$, $H_2O$, $CO_2$ etc) scatter radiation according to Rayleigh’s law (molecular scattering) and absorb them. The principal atmospheric components affecting the top-of atmosphere (TOA) or at-satellite-reflectance are shown in Figure.1. The atmospheric correction requires inputs that describe these variable constituents that influence the signal at the top of the atmosphere.

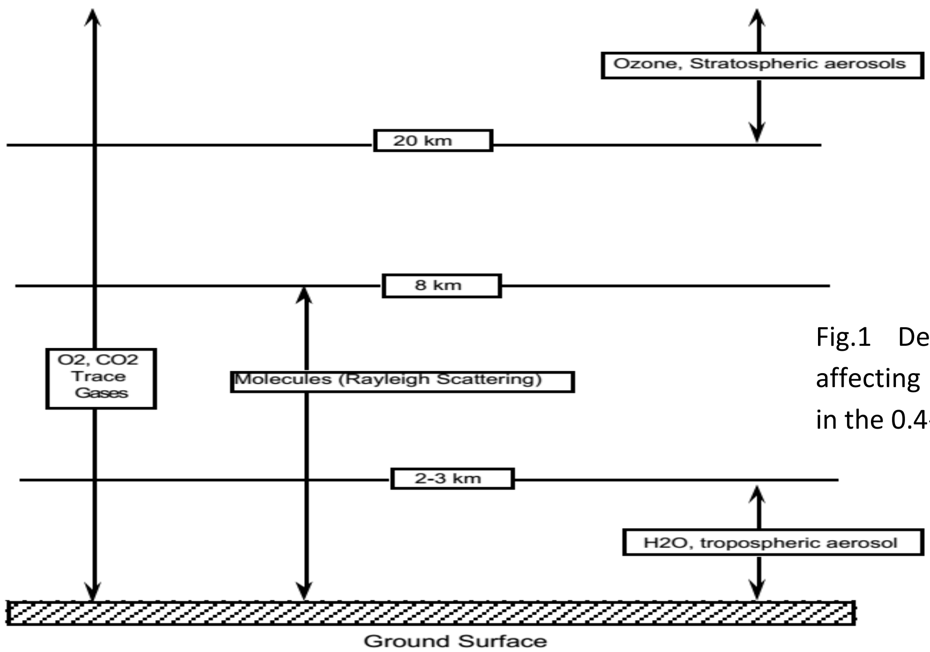


Fig.1 Description of components affecting the remote sensing signal in the 0.4-2.5 µm range.

**Second Simulation of Satellite Signal in the Solar Spectrum (6S):**

The 6S code is a basic RT code used for calculation of lookup tables in the MODIS (Moderate Resolution Imaging Spectro-radiometer) atmospheric correction algorithm. It enables accurate simulation of satellite and airborne observations, accounting for elevated targets, use of anisotropic and Lambertian surfaces, and calculation of gaseous absorption. The new vector version of the code can operate in both scalar and vector modes. The 6S code is based on the method of successive orders of scattering (SOS) approximations. In 6S the atmosphere is divided into a number of layers and the RT equation is solved numerically for each layer with the help of iterations. The intensity is successively computed for photons scattered once, twice, three times, and etc. with the total intensity obtained as the sum of all orders. Numerical integration is performed using the decomposition in Fourier series for the azimuth angle and Gaussian quadratures for the zenith angle. This code predicts a satellite signal at λ = 0.25 - 4.0 μm assuming cloudless atmosphere with a fixed resolution of 10 $cm^{-1}$. 6S atmospheric simulation model reduces the uncertainties in the process of electromagnetic wave transmission and effectively eliminates the perturbation from geometric- and system-corrected remote sensing imagery. 6S was developed specifically for satellite applications and the user can define only a downward-looking geometry. Unlike other codes, which allow just one, 6S offers two main working modalities:

• Simulation: the model generates an atmospheric background and returns transmittance values, top of atmosphere (TOA) reflectance/radiance and all values used to resolve a RT problem;

• Atmospheric correction: in this modality 6S solves the RT problem back-to-front. Given a TOA reflectance/radiance it provides correction coefficients to compute at-ground reflectance/radiance.

Moreover the last release of 6S allows performing simulations both in scalar and in vector mode, considering in this last case Stokes' Parameters and Light polarization contributes.6S model can simulate the solar radiation on the ground and in the atmosphere from 0.2 μm to 4.0 μm spectral range under a variety of conditions of both ground surface and atmosphere. Assuming a uniform Lambertian ground surface and if gaseous absorption can be de-coupled from scattering as if the absorbents were located above the scattering layers, the equation of transfer for homogeneous target of reflectance as viewed by a satellite sensor (under zenith angle of view θv azimuth angle of view φv) and illuminated by sun (θs,φs )[6]

$$\rho_{TOA}(\theta_s, \theta_v, \varphi_s - \varphi_v) = T_g(\theta_s, \theta_v)\left[\rho_{R+A} + T\downarrow(\theta_s)T\uparrow(\theta_v)\frac{\rho_s}{1-S\rho_s}\right] \text{---------(1)}$$

where reflectanceρ defined as

$$\rho = \frac{\pi L}{\mu_S E_S} \text{--------------------(2)}$$

where L is the measured radiance, $E_s$ is the solar flux at the top of the atmosphere, and $\mu_s = \cos(\theta_s)$ where $\theta_s$, is the solar zenith angle.

In equation(1),$\rho_{TOA}$- Apparent Reflectance measured at the top of the atmosphere, $\rho_{R+A}$ corresponds to the intrinsic reflectance of the molecule+aerosol layer, $T\downarrow(\theta s)$, [respectively $T\uparrow(\theta v)$] to the total transmission of the atmosphere on the path between the sun and the surface, (respectively between the surface and the sensor). S is the spherical albedo of the atmosphere i.e., the normalized irradiance backscattered by the atmosphere when the input irradiance at the bottom is isotropic. Tg is the gaseous transmission, for the solar radiation

## 2.2 Inputs

Atmospheric correction using 6S code requires the following input parameters (1) geometrical conditions, (2) the atmospheric model for gaseous components, (3) the aerosol model (type and concentration), (4) spectral condition, and (5) ground reflectance (type and spectral variation). Table (1) lists the options chosen for arriving at the geometric, atmospheric and sensor parameters needed to run the 6S models.

| Parameter | Specific Input Required | General Input Chosen |
|---|---|---|
| Geometrical Conditions | Date and Month<br>View and Sun angles (in °) | User's |
| Atmospheric Model | Water vapor(g/cm$^2$), ozone(cm-atm),<br>AOD at 550nm | Uw and $UO_3$<br>Continental Aerosol Model |
| Spectral Condition | Lower and upper wavelengths of the spectral band in µm | User's preference |
| Target and Sensor Altitude | Sensor Altitude in Km<br>Target Altitude: sea level | |
| Ground Reflectance | | Homogenous ground<br>No Directional effect |

Table1. Parameters option chosen to run the 6S model

The geometrical parameter which includes the sun and view, zenith and azimuth angles were derived from the image itself. Accurate atmospheric parameters are crucial for transferring top-of-atmosphere (TOA) radiance or reflectance to surface reflectance products. MODIS atmospheric products were used to generate atmospheric parameters. AOD (Aerosol Optical Depth) values used from MODIS (MOD04_L2) which is available at 0.1° x 0.1° spatial grid daily. While the ozone and water vapour values were derived from MODIS joint atmospheric product, namely MOD07_L2 which is defined on 0.05° × 0.05° grid cells that cover the entire globe.

## 2.3 Implementation of algorithm

6SV1.2 modules were downloaded (https://salsa.umd.edu/6spage.html), successfully installed and tested against various combinations of inputs. Using the above mentioned parameter models; the 6S code was used to obtain the correction coefficients which are further used to derive the surface reflectance from the measured radiance values. The flow-chart in Fig.(2) Illustrates the procedure followed to arrive at the surface reflectance products. The 6S coefficients are generated for each input grid by taking satellite/sun azimuth/elevation values, Aerosol Optical Depth (AOD), Water vapour and Ozone values over that grid.

For each input spectral band, the 6S code generates three correction coefficients namely xa, xb and xc. The equation to obtain $\rho_s$ from these correction coefficients is given by

$$\rho_s = (xa * L - xb)/[1.0 + xc\ (xa * L - xb)] \qquad \text{-------------(3)}$$

Where xa, xb and xc are the coefficients obtained from the 6S model, where, xa is the inverse of the transmittance and xb is the scattering term of the atmosphere and xc is the reflectance of the atmosphere for isotropic light entering the base of the atmosphere [10]. The number of times the 6S code is called for the generation of surface reflectance products typically depends on the grid size. The software provides an option for flexible grid sizes namely, 100 X 100, 200 x 200 or 300x 300. The correction coefficients are stored as an image of 3 layers (xa, xb and xc). Finally surface reflectance was calculated pixel by pixel using the output coefficients, by applying the same values of output coefficients for all the pixels falling in the same grid. The output coefficients are computed for each band.

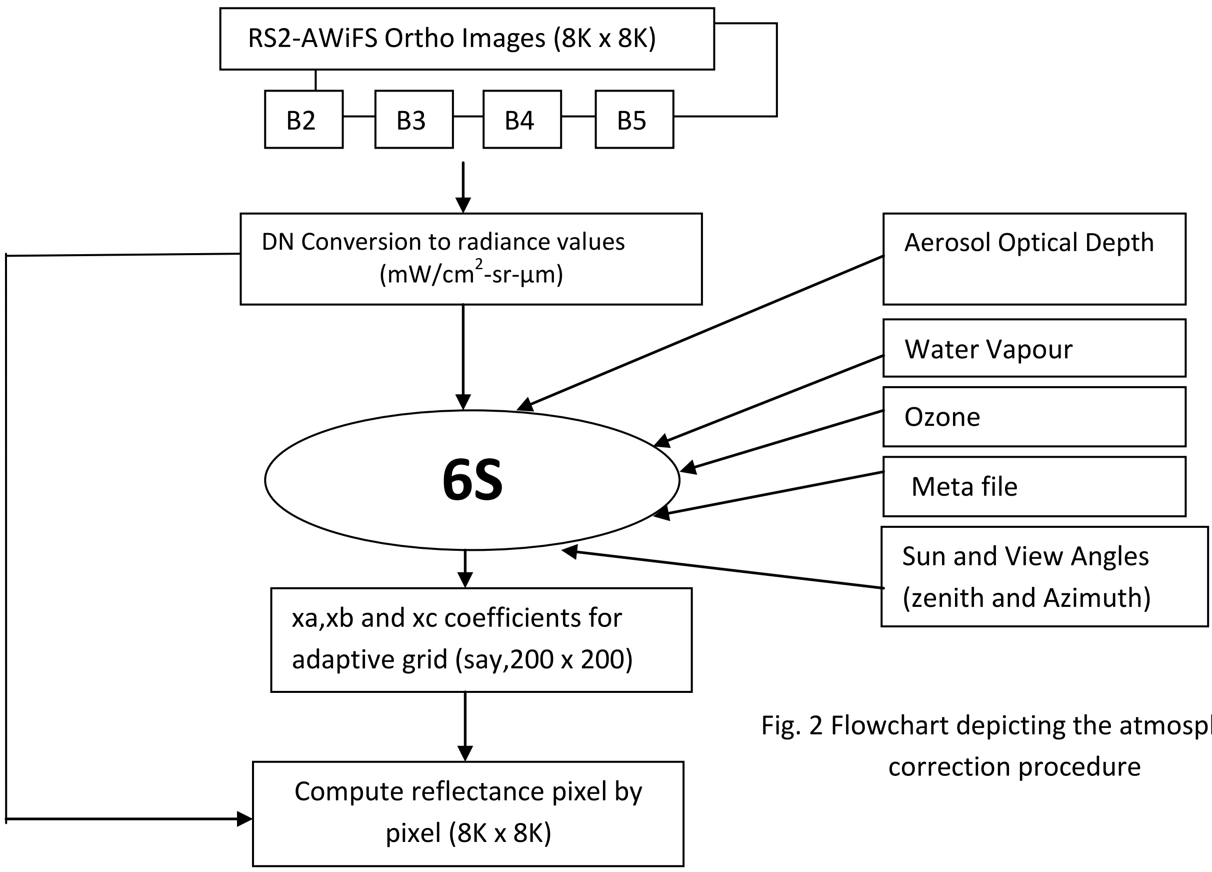


Fig. 2 Flowchart depicting the atmospheric correction procedure

All software modules (**ACT** – **A**tmospheric **C**orrection **T**ool) are developed and tested using Java programming language. The calculation for each pixel is independent of each other and can be carried out in parallel. So multi-threading concepts were used and the same was implemented on 4*22 cores CPU machine to achieve high throughput and reduced turnaround time (TAT) of product generation.

The Fig.3 displays the GUI which integrates the atmospheric profile data, Meta data along with RS2 sensor data to arrive at the surface reflectance product.

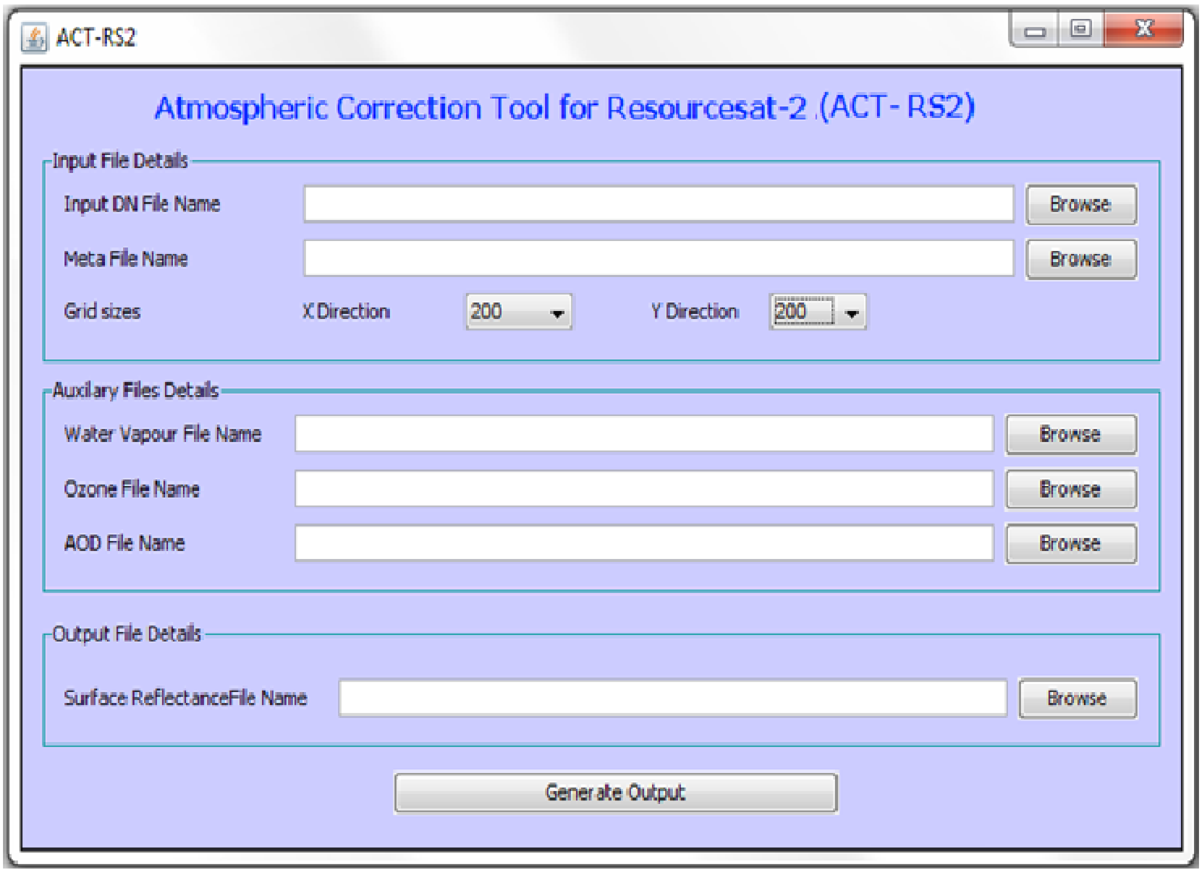


Fig. 3 Snapshot of GUI developed for atmospheric correction of RS2 AWiFS

# 3.0 Results and Validation: 2015, 2016 and 2017 data.

## 3.1 Differences between TOA and surface reflectance for RS2 AWiFS and LISS-3 Data

To determine the effects of atmospheric correction, a visual comparison of ROIs extracted from TOA and surface reflectance images was undertaken with false-colour images. The TOA (Figure 4A) and surface reflectance (Figure 4B) images appear quite different: there is less visual contrast in TOA reflectance due to the impact of the atmosphere

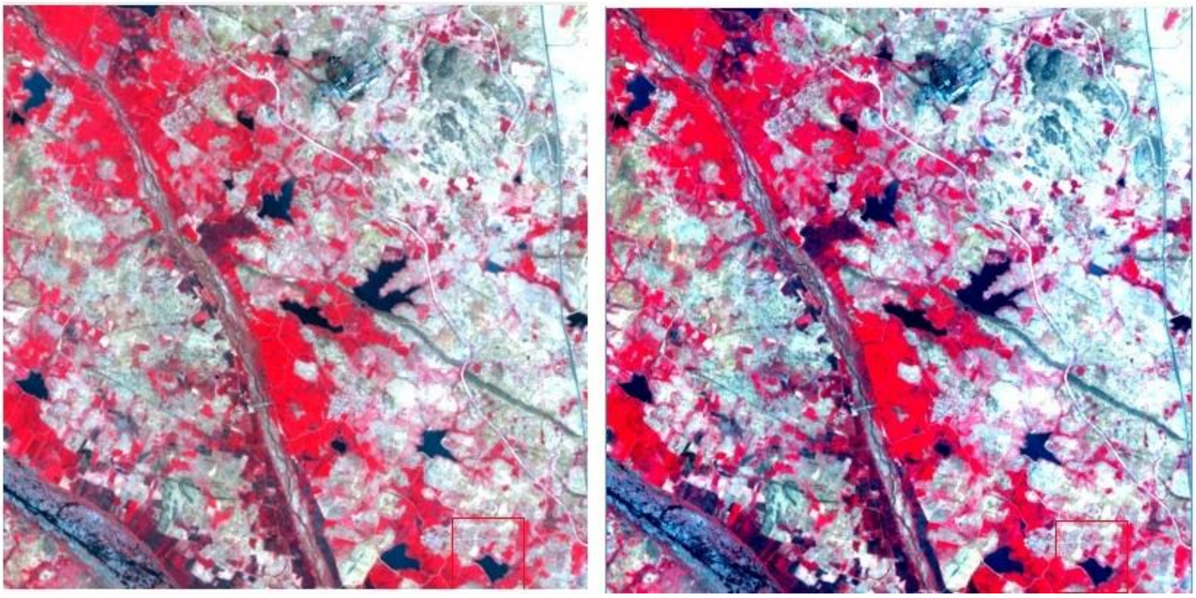

Fig. 4A Color composite of LISS-3 ROI band3 (R), band2 (G), band1 (B) imagery acquired on 16Feb2016 for path 100_61 (a) before and (b) after atmospheric correction

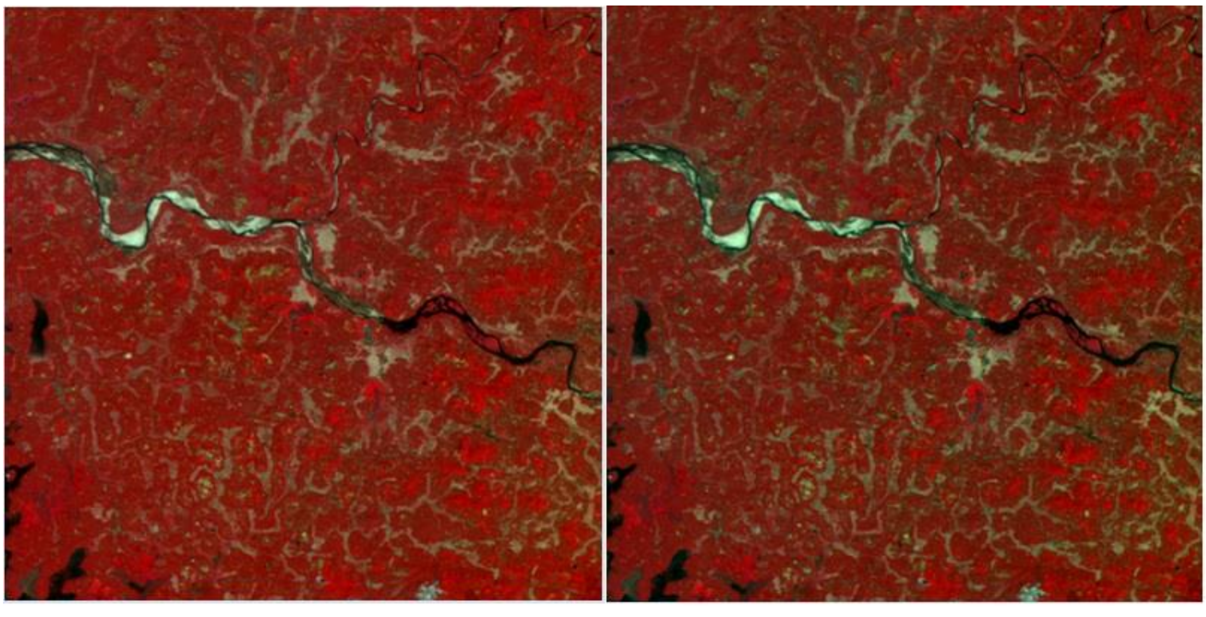

Fig. 4B Color composite of AWIFS ROI band3 (R), band2 (G), band1 (B) imagery acquired on 16Feb2015 for path 99_69_A (a) before and (b) after atmospheric correction

The difference is further quantitatively estimated by comparing the histogram of both corrected and uncorrected images. The histograms of uncorrected TOA reflectance compared with the corresponding atmospherically corrected for AWiFS image (99_59_A_16thfeb2015) for each spectral band (fig.4). It is evident that the atmospheric correction has smoothened all the four histograms. The values of surface reflectance were lower than the TOA reflectance in visible bands. It shows that the TOA reflectances are corrected for the scattering effects which are predominant in these wavelengths. The impact of the atmosphere on the SWIR bands was obviously less than for the other bands. Also spread in histogram of surface reflectance image confirms a contrast improvement of the atmospherically corrected image by reducing the response of the lower reflecting targets(< 0.15%) and increase in reflectance of higher reflecting targets (> 0.15%) .

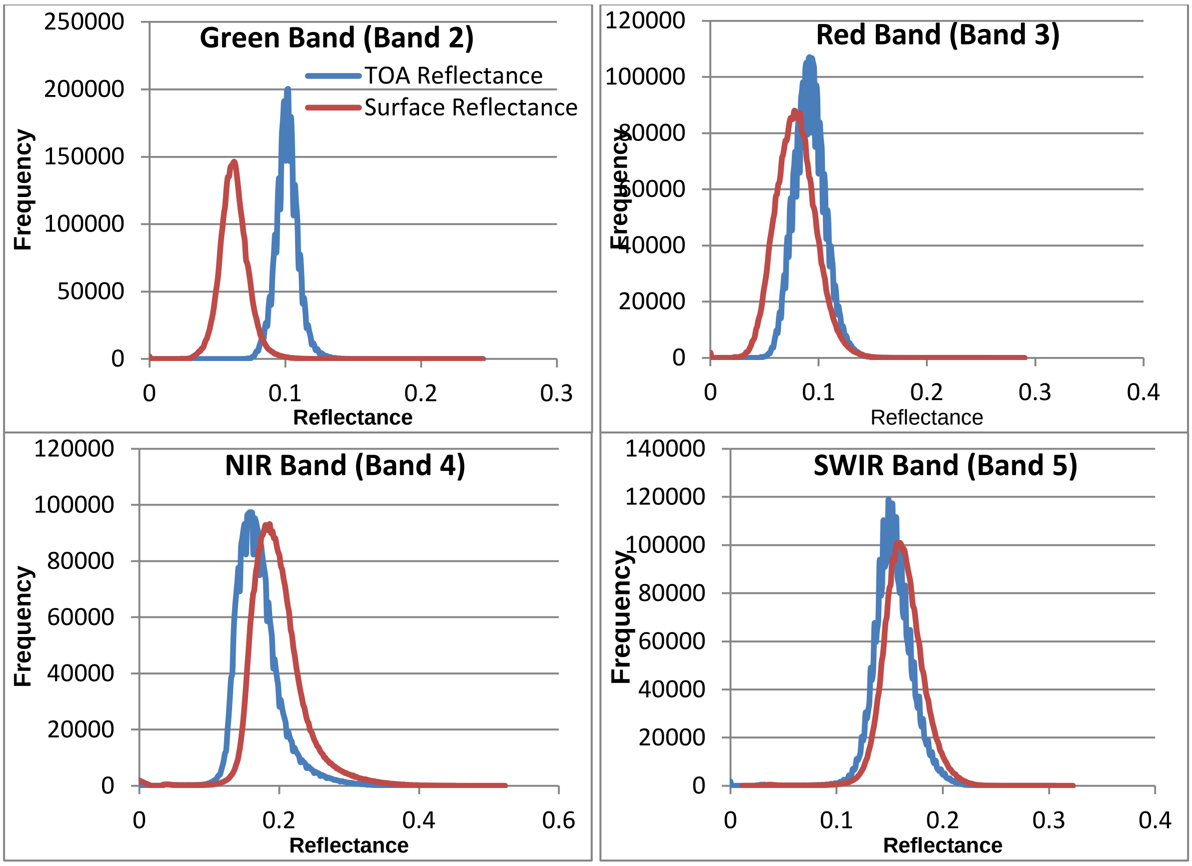


Fig5. Histograms of reflectance in AWIFS images before and after atmospheric

## 3.2 Validation with Ground Data

The accuracy of the 6S atmospheric correction algorithm was validated using ground radiometric measurements over IMGEOS cal-val site, Thar Desert and over ICRISAT Hyderabad. The aggregated ground measurements were converted into AWiFS and LISS-3 sensor's reflectance using the respective spectral response function of sensor bands. The results of comparisons for red and black soil features of IMGEOS cal-val site and ICRISAT vegetation are shown in Fig (6A, B) below.

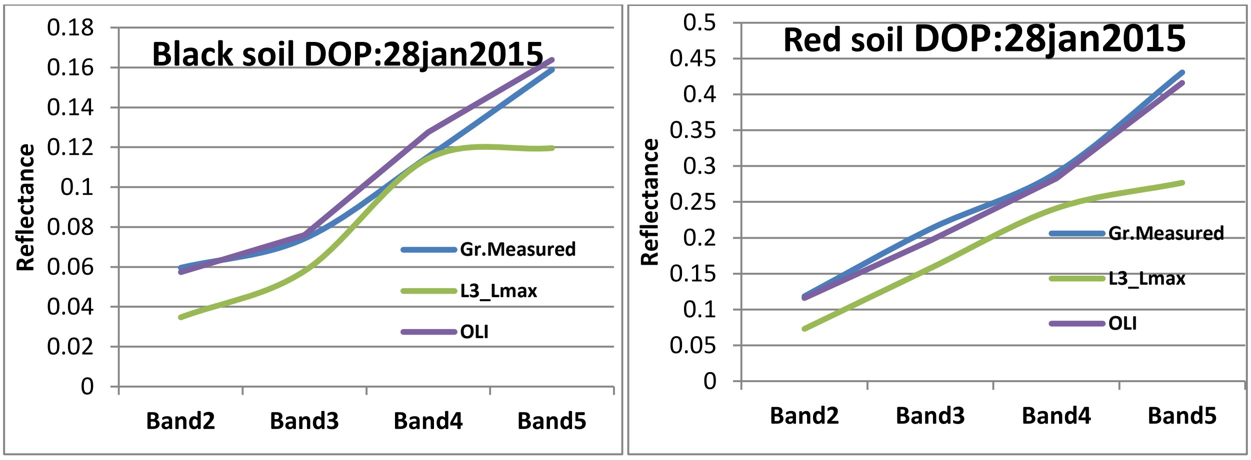


Fig6A. Validation of LISS-3 surface reflectance with aggregated spectro-radiometer measurements over cal-val site IMGEOS

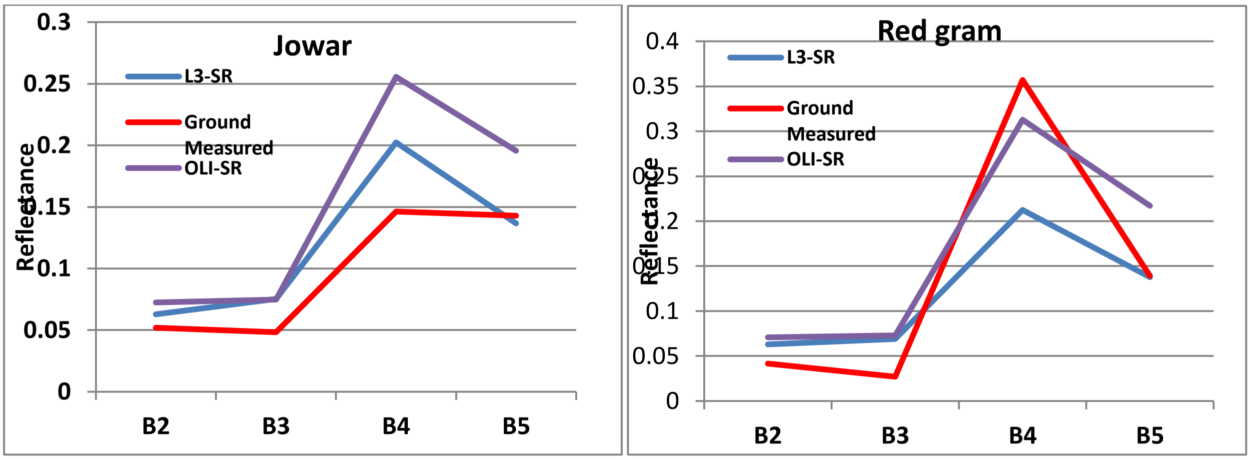


Fig6B Validation of LISS-3 surface reflectance with aggregated spectroradiometer measurements for vegetation

Scatter plots between the LISS-3 surface reflectance and spectro-radiometer measurements acquired on five different dates in the year 2015 over different targets of the IMGOES cal-val site confirms that LISS-3SR are consistent with spectro-radiometer readings(fig.7)

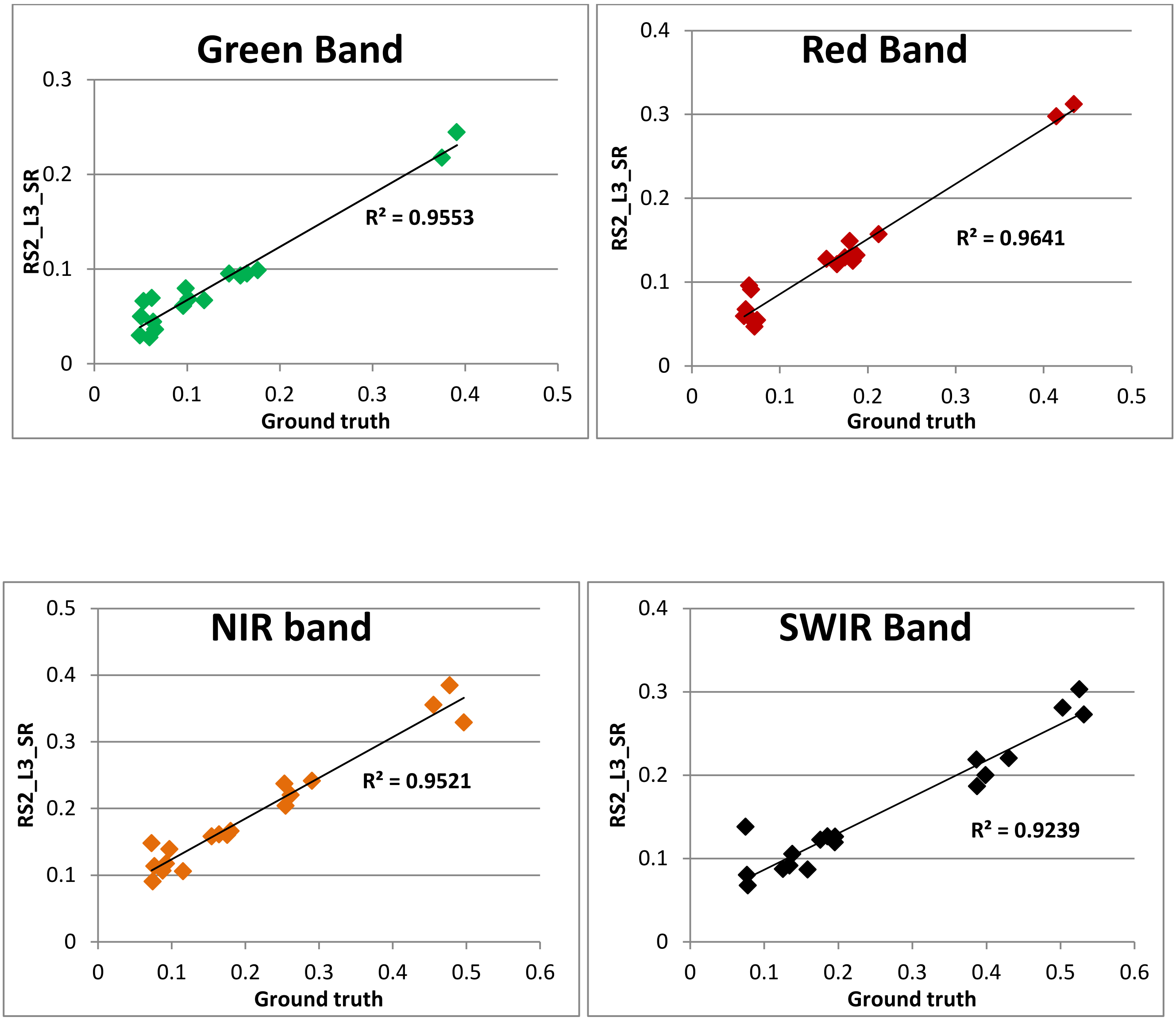


Fig.7 Validation of the retrieved LISS-3 reflectance and the aggregated spectro-radiometer readings acquired on four dates (Jan 28, Nov 12, Dec 25, Dec 30 of 2015)

AWiFS Surface reflectance data was compared with ground measured spectro-radiometer data over Thar Desert area. Data sets used for the validation were collected during the months of Nov'11, Dec'11 and Dec'12. Results of validation are shown in Fig8. $R^2$ value for all the four bands were greater than 85%.

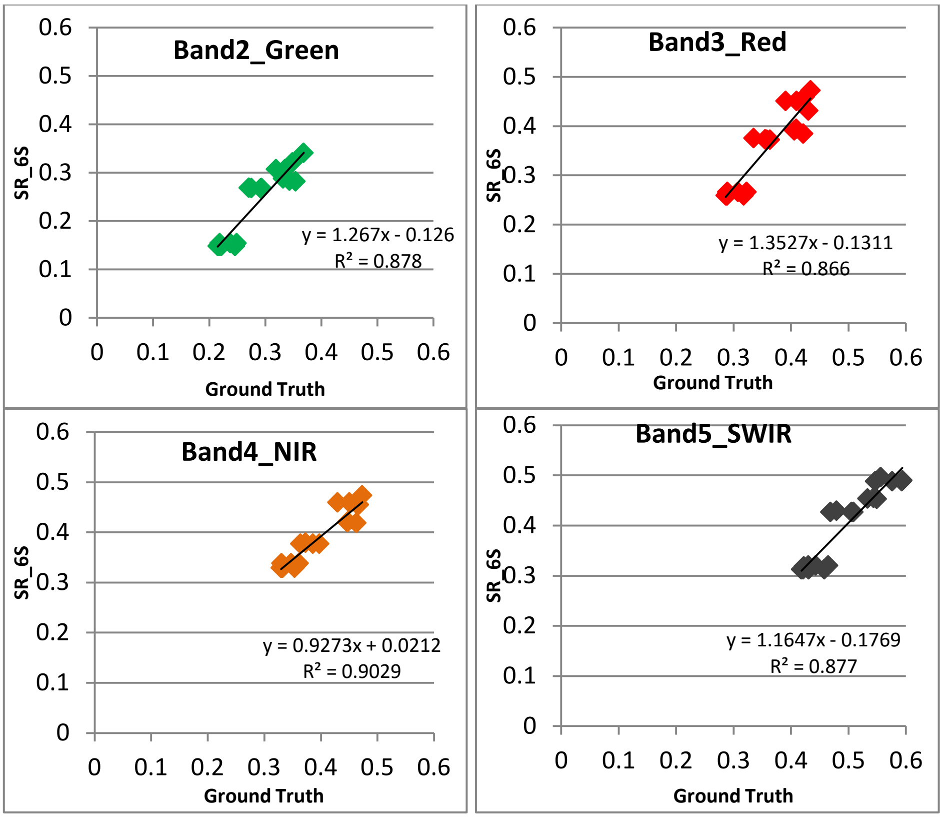


Fig.8 Validation of desert sand AWiFS surface reflectance with ground spectral data

## 3.3 Validation using Landsat-8 Data

In addition to making comparisons with ground observations, the quality of Resourcesat 2 surface reflectance data were also assessed using Landsat8 OLI surface reflectance product. LISS-3 surface reflectance products were compared with contemporaneous L8 OLI images over heterogeneous targets like river sand(Allahabad Prayaga), desert(Thar), ever green forest, agriculture fields(Punjab, Andhra Pradesh, water(Kurukshetra lake, Manasarovar) , urban(Delhi, Bangalore) etc. The fig.9 presents the results of comparisons.

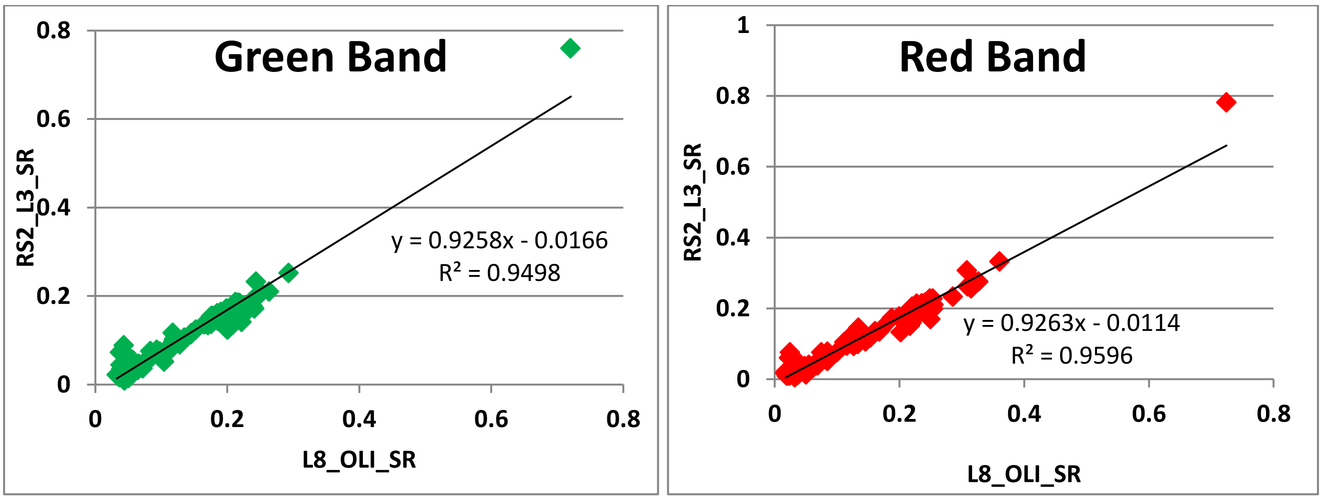

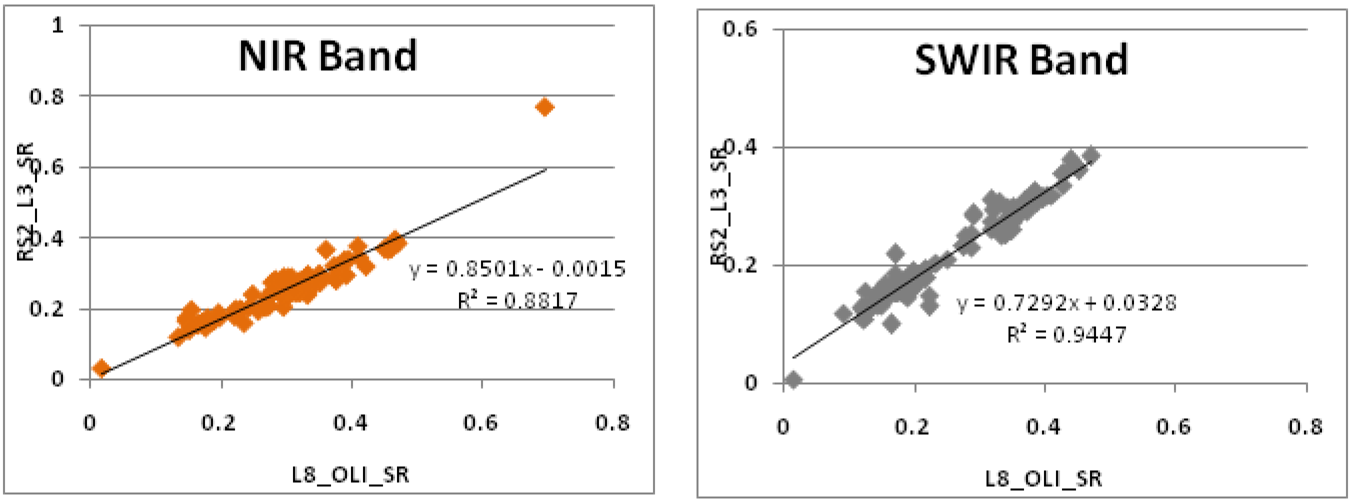


Fig.9 Scatter plot of surface reflectance between LISS-3 and OLI for heterogeneous targets acquired on multiple

Similar studies were carried out on AWiFS image also. Scatter plot comparing the surface reflectance of OLI and AWiFS data is displayed in Fig.10 below.

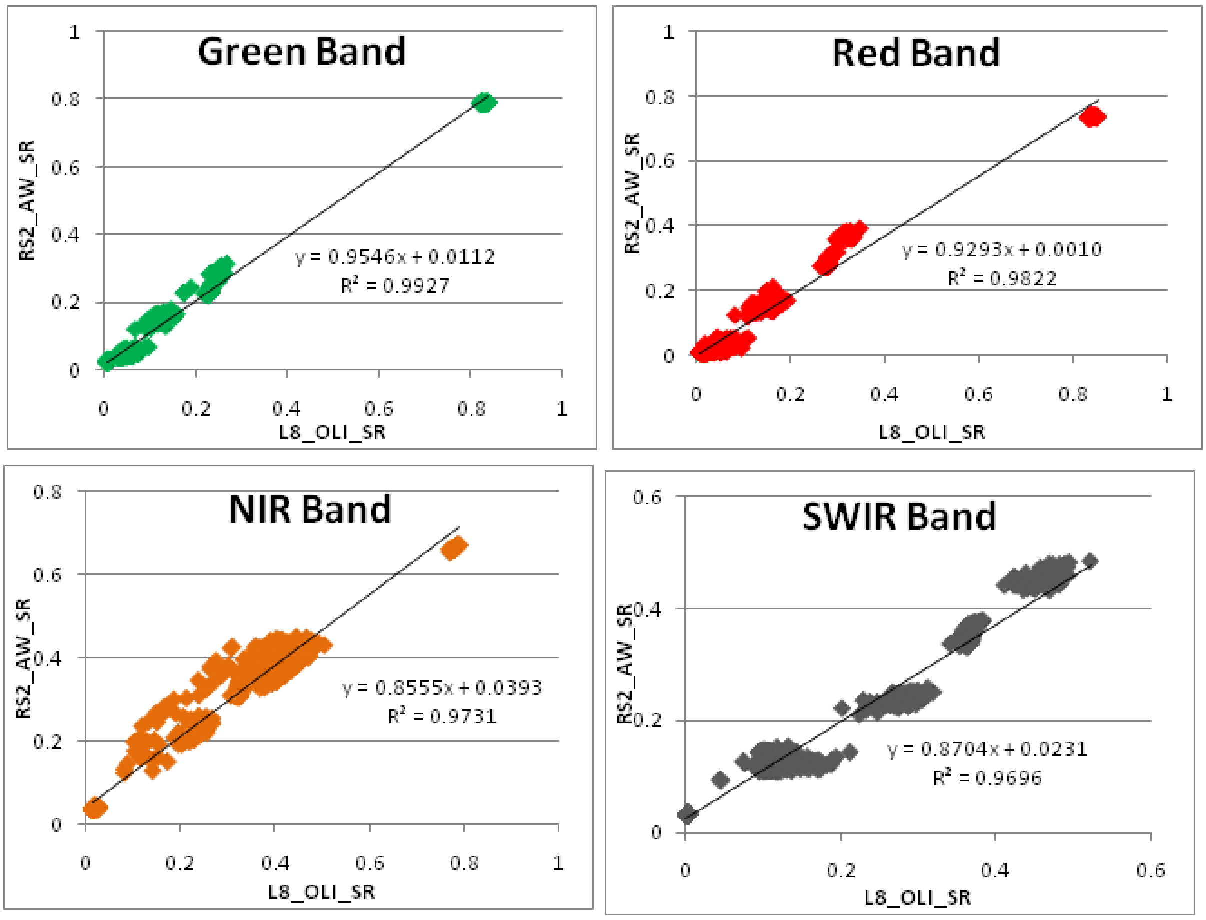


Fig10 Scatter plot of surface reflectance between AWiFS and OLI for heterogeneous targets acquired on multiple dates

In order to evaluate the differences and correlation between L8 OLI and RS2 (LISS-3 and AWiFS ) surface reflectance $R^2$ values, RMSE (Sqrt($\sum(\rho_{L8} - \rho_{L3})^2/N$)), and maximum absolute deviations (abs($\rho_{L8} - \rho_{L3}$) ) were calculated for the four bands(Table 2A and 2B).The RS2 surface reflectance values were found to be close to L8 OLI surface reflectance values with mean $R^2$ of 0.9335 and RMSE ranging from 0.34 to 0.062 for LISS-3 sensor . Linear Regression of AWiFS surface reflectance products with L8 OLI surface reflectance products had mean $R^2$ value of0.9252 and RMSE ranged from 0.17 to 0.38.

| | **$R^2$** | **RMSE** | **Max. Abs. Deviation** |
|---|---|---|---|
| **Green Band** | 0.9498 | 0.0369 | 0.0692 |
| **Red Band** | 0.9596 | 0.0341 | 0.0665 |
| **NIR Band** | 0.8817 | 0.0623 | 0.0887 |
| **SWIR Band** | 0.9447 | 0.0465 | 0.0760 |

Table 2A. $R^2$, RMSE and max. absolute deviations of LISS-3 SR value with respect to OLI SR

| | **$R^2$** | **RMSE** | **Max. Abs. Deviation** |
|---|---|---|---|
| **Green Band** | 0.9927 | 0.0169 | 0.0039 |
| **Red Band** | 0.9822 | 0.0261 | 0.0232 |
| **NIR Band** | 0.8555 | 0.0383 | 0.0116 |
| **SWIR Band** | 0.8704 | 0.0239 | 0.068 |

Table 2B. R2, RMSE and max. absolute deviations of AWiFS SR value with respect to OLI SR

reflectance with L8 OLI surface reflectance products were also carried on images which are having a nearby date of pass. The results are displayed in Table 3Aand 3B.

| **LISS-3 Sub scene** | **OLI sub scene** | **Correlation Coefficient r for** | | | |
|---|---|---|---|---|---|
| | | **Green Band** | **Red Band** | **NIR Band** | **SWIR Band** |
| 90_55_26may'15 | 151_43_22may'15 | 0.9369 | 0.9430 | 0.9480 | 0.9816 |
| 90_55_25sep'15 | 150_39_17sep'15 | 0.8235 | 0.8461 | 0.8675 | 0.8311 |
| 102_61_05oct'15 | 142_49_28sep'15 | 0.9538 | 0.9558 | 0.8735 | 0.9027 |
| 100_61_16feb'16 | 144_48_17feb'16 | 0.9483 | 0.9469 | 0.9047 | 0.9081 |

Table 3A Correlation Coefficient associated with all bands of LISS-3 sensor with respect

| **AWiFS Sub Scene** | **OLI Sub Scene** | **Correlation Coefficient r for** | | | |
|---|---|---|---|---|---|
| | | **Green Band** | **Red Band** | **NIR Band** | **SWIR Band** |
| 104_60_A_17FEB'15 | 142_46_16FEB'15 | 0.9688 | 0.9666 | 0.9862 | 0.9580 |
| 99_48_A_30MAR'16 | 146_36_03APR'16 | 0.9717 | 0.9693 | 0.9729 | 0.9548 |
| 095_58_D_20FEB'15 | 145_47_21FEB'15 | 0.9575 | 0.9615 | 0.9577 | 0.9539 |
| 100_62_B_16FEB'16 | 144_48_17FEB'16 | 0.9851 | 0.9732 | 0.9615 | 0.9066 |

Table 3B Correlation Coefficient associated with all bands of AWiFS sensor with

All four band of LISS-3 and AWiFS sensor are well correlated with L8 OLI bands with average correlation coefficient more 0.9.

## 3.4. Intra sensor validation

Intra sensor validation was also carried out by comparing AWiFS and LISS-3 surface reflectance values acquired on the same day. The following figure (8) compares the surface reflectance values for the path 93_49 for LISS-3 and 93_48 for AWiFS acquired on 10 Feb 2015.

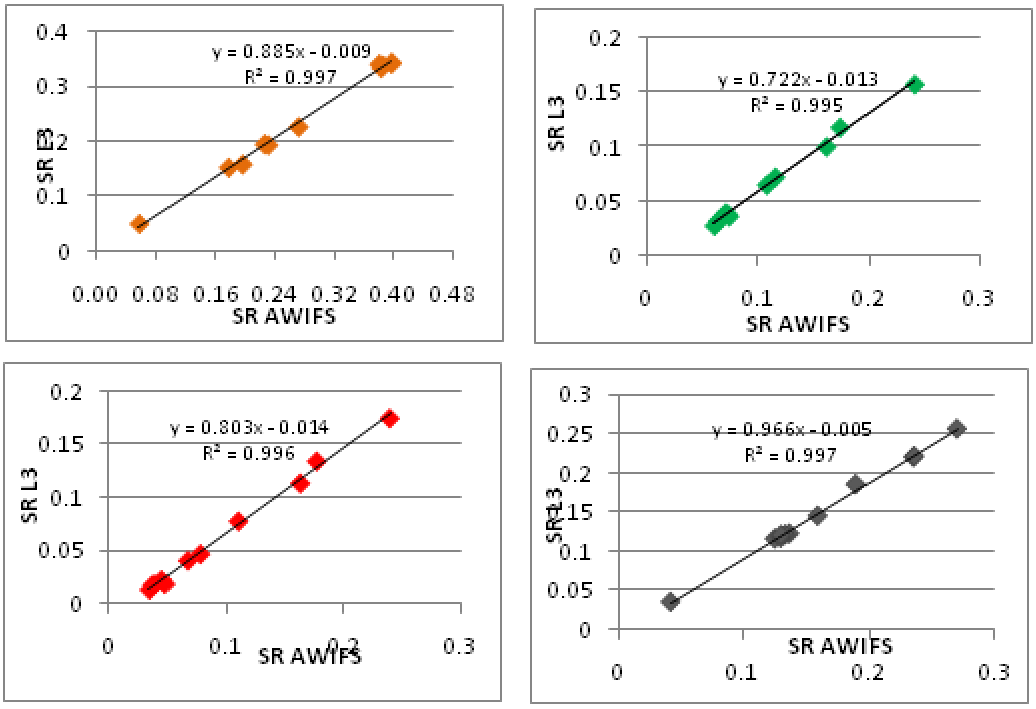


Fig.11. Scatter plot of LISS-3 and AWiFS Surface reflectance

The results confirm that the values are well distributed near the 1:1 line with $R^2$ value greater than 0.99 for all the bands.

# 4. Application of Atmospheric correction

In order to evaluate the effect of atmospheric correction in the generation of information products, the NDVI values of vegetated pixels before and after atmospheric correction in AWIFS images are compared. The result of the analysis is shown in Fig.8.

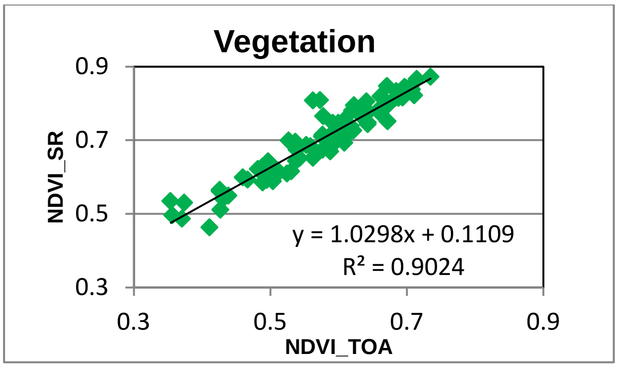


Fig.12. Scatter plot of NDVI values before and after atmospheric correction

It is conspicuous from the slope greater than one and positive offset that the atmospheric correction has increased the NDVI values. The observed pattern matches to already reported fact the NDVI calculated from apparent reflectance is the lowest while the NDVI derived from surface reflectance values are much higher[11]. Atmospheric effects tend to reduce the NDVI and NDVI derived from surface reflectance products can better account for the vegetation vigour. The effect is further illustrated on LISS-3 NDVI images acquired on 05 Oct 2015 for Punjab region.

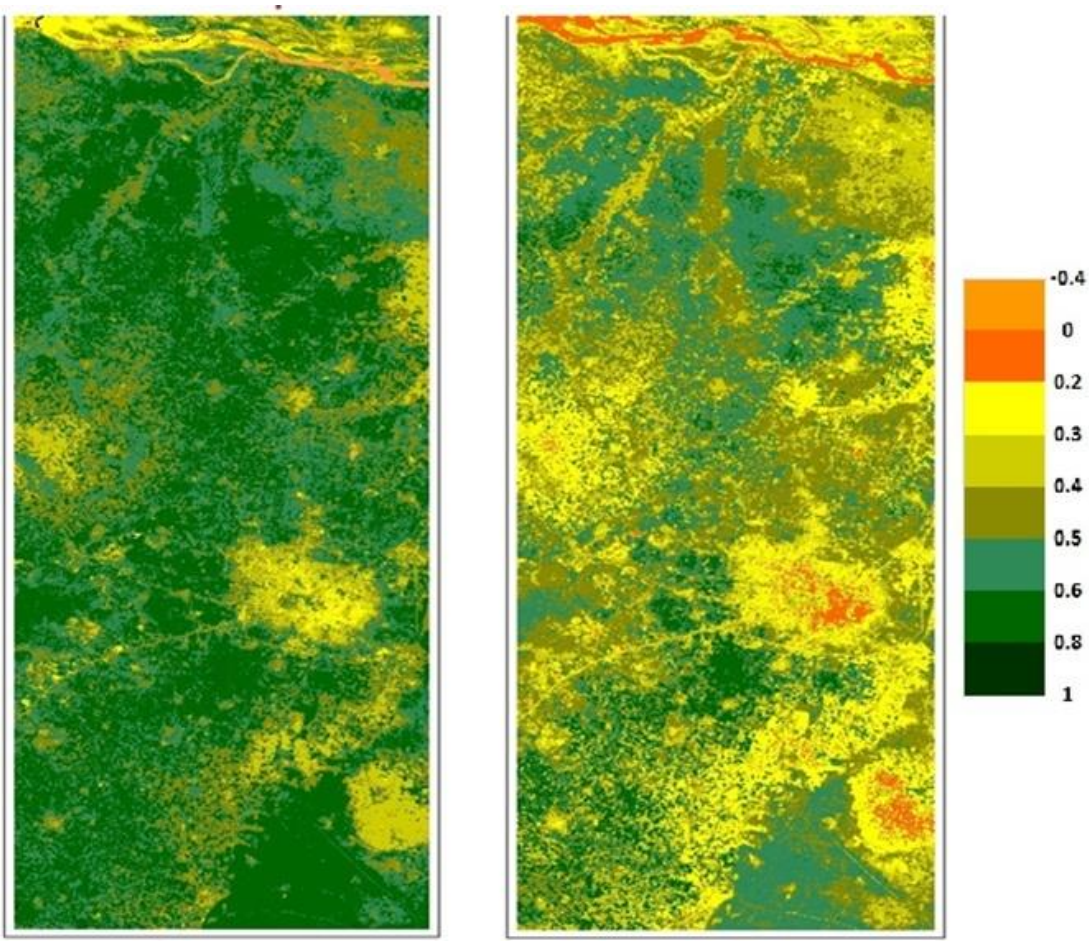


Fig.13 NDVI images before and after atmospheric correction

NDVI image (left) in fig.10 which is derived from atmospherically corrected image has higher NDVI values as compared to NDVI image (right) derived from TOA values. Histogram of NDVI images (fig.11) also confirms the improvement achieved by atmospheric correction.

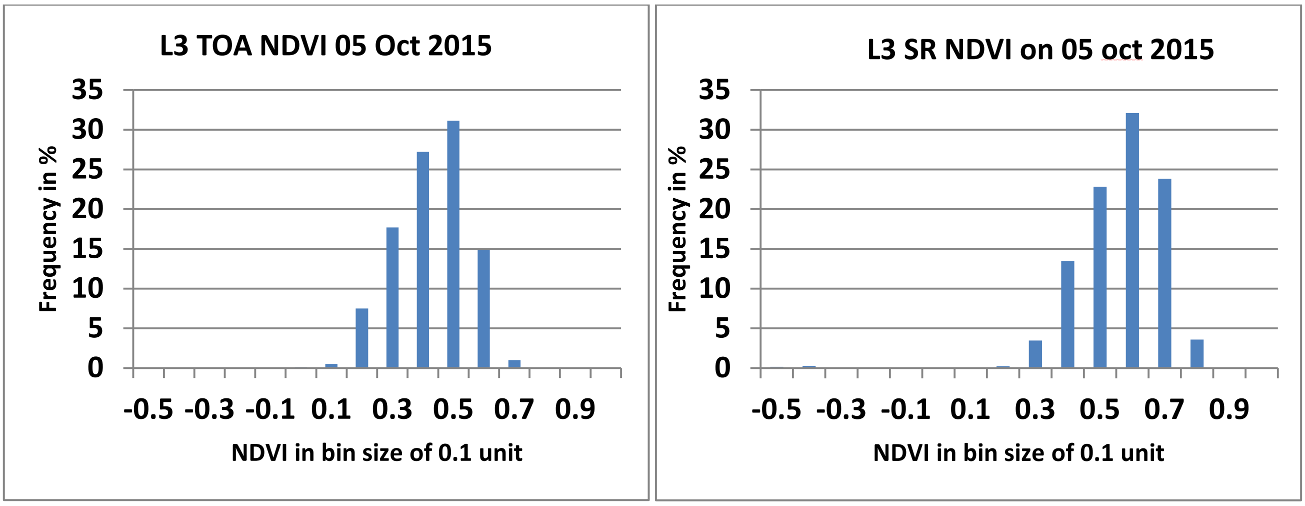


Fig.14 Histogram of NDVI images before and after atmospheric

## 5.0 Results and Validation on 2020 datasets.

As mentioned in section 3.0 surface reflectance datasets of latest 2020 RS2/2A were generated using the proposed methodology and were compared against Landsat-8 OLI near synchronous SR images.

For each of the four RS2/2A LISS-3 and AWiFS multispectral bands, there is a L8 OLI band with a spectral range well within that of the corresponding RS-2/2A band. Table 4 compares the bandwidth of bands available in Landsat8 OLI and RS2/2A AWiFS. The USGS provisional Landsat-8 SR product is corrected based on an internal model and the MODIS Climate Modelling Grid (CMG) atmospheric product. The OLI SR products are available for free downloads from https://earthexplorer.usgs.gov.

| | **Landsat8 OLIBW in µm** | **RS2/2A AWIFS and LISS 3 BW in µm** |
|---|---|---|
| **Green band** | Band30.53-0.59 | Band20.52-0.59 |
| **Red band** | Band40.64-0.67 | Band30.62-0.68 |
| **NIR band** | Band50.85-0.88 | Band40.77-86 |
| **SWIR band** | Band61.57-1.65 | Band5 1.55-1.70 |

Table4: The 4 multispectral bands of the RS-2 LISS 3 and AWiFS sensors and the corresponding L8 OLI bands.

AWiFS and LISS 3 data with a spatial resolution of 56m and 24m respectively are comparable with 30m resolution of L8 OLI data. Earlier, validations were carried with many numbers of scenes covering various ground targets from RS2 AWiFS and LISSS 3 sensors acquired in the years 2015, 2016, 2017. Presently, validation was carried out with 12 scenes of both RS2 and

2A as listed in Table 5. Images were selected so as to include a wide variety of target reflectance from lesser reflecting water targets to highly reflecting river sand and snow.

## 5.1 Results of Cross comparison of RS2/2A AWiFS, LISS 3 SR products with L8 OLI SR products

The SR images generated were compared with Landsat 8 OLI SR images acquired over the same period with a margin of 3 -5 days on either side. Depending on the homogeneity of the scene minimum of 500 to maximum of 5000 pixels were randomly selected from each of the scene. A scatter plot is produced for each individual RS-2/2A AWiFS, LISS 3 band with L8 OLI band for the different targets. A linear regression (black line) was then calculated to represent the differences in surface reflectance between L8 and RS-2/2A pixels. In each scatter plot, L8 OLI SR values are represented on the x-axis; RS-2/2A AWiFS, LISS 3 SR values are represented on the y-axis; respectively. The 1:1 line (red line) is also added to each chart as in figures 15 to 18. Figures 15 &16 represent the variation in AWiFS sub scenes of RS-2 and 2A with respect to L8 surface reflectance over various targets like vegetation, desert sand water and urban area. Figures 17 & 18 represents the variation in RS2 and 2A LISS 3 surface reflectance over vegetation, urban areas, desert sand, water bodies.

| Satellite/Sensor | Path-Row-Sub scene-DOP | OLI -L8 |
|---|---|---|
| **RS2 AWiFS** | 090-054-A-22feb2020 | 150-41-22feb2020<br>150-42-22feb2020 |
| | 090-054-B-22feb2020 | 150-41-22feb2020<br>150-42-22feb2020 |
| **RS2 LISS 3** | 092-044-03mar2020 | 149-34-02mar2020<br>149-35-02mar2020 |
| | 090-054-22feb2020 | 150-41-22feb2020<br>150-42-22feb2020 |
| | 101-061-24mar2020 | 143-48-24mar2020<br>143-49-24mar2020 |
| | 090-052-28may2020 | 150-41-28may2020<br>150-42-28may2020 |
| | 090-053-28may2020 | 150-41-28may2020<br>150-42-28may2020 |
| | 102-060-29mar2020 | 142-48-02apr2020 |
| **RS2A AWiFS** | 093-051-C-20feb2020 | 150-41-22feb2020 |
| **RS2A LISS 3** | 093-051-20feb2020 | 150-41-22feb2020<br>150-42-22feb2020 |
| | 092-049-15feb2020 | 149-38-15feb2020<br>149-39-15feb2020<br>149-40-15feb2020 |
| | 092-050-03apr2020<br>092-051-03apr2020 | 149-39-03apr2020<br>149-40-03apr2020 |

Table5. Details of selected scenes (Path, Row, Sub scene, Date of pass) for RS2/2A and OLI-L8

Table 6(page 47) lists the slope, offset and coefficient of determination $R^2$ values for all the four bands for each scene. The slope was close to 1 in most cases except snow targets present in the scene on 03rd march 2020 and offset values were close to 0. There is an ambiguity in ancillary data over snow region, hence SR values of snow targets are not matching with L8 SR values and also some of the SR values of L8 are saturated for snow target. The $R^2$ values were also more than 90% in most of the cases.

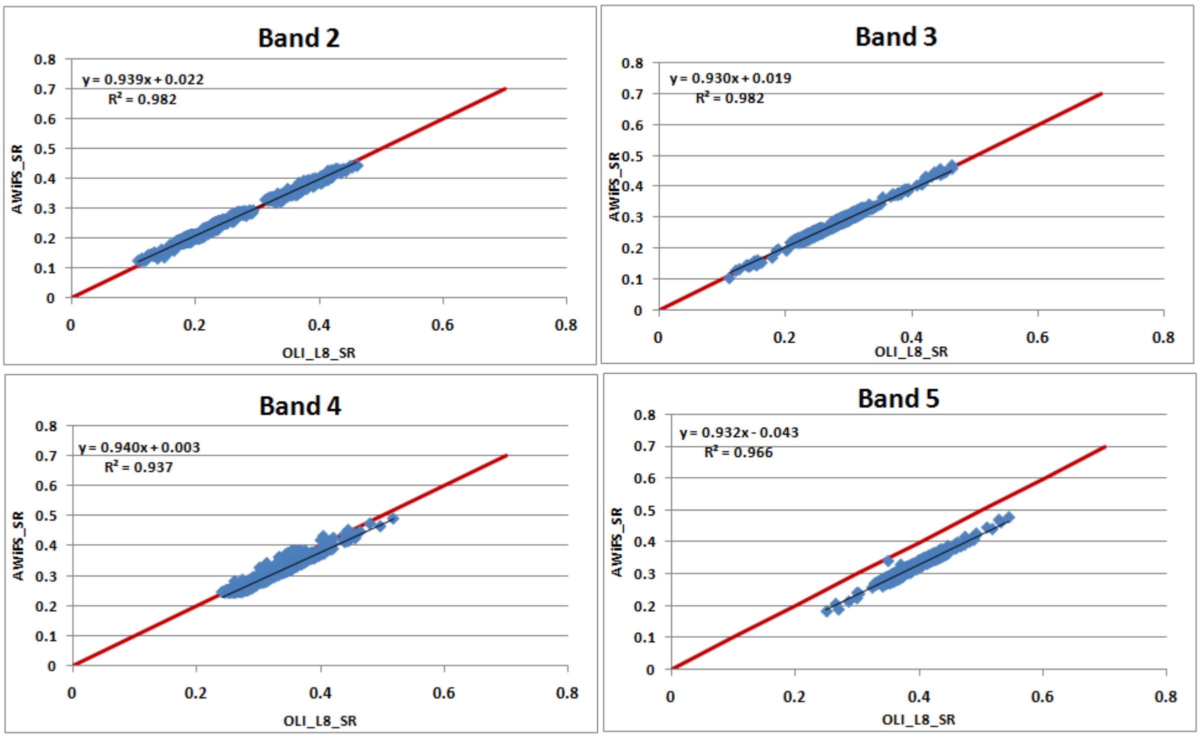


Fig.15 Scatter plot between RS2 AWiFS-A SR and OLI-L8 SR for each band DOP:22 Feb2020

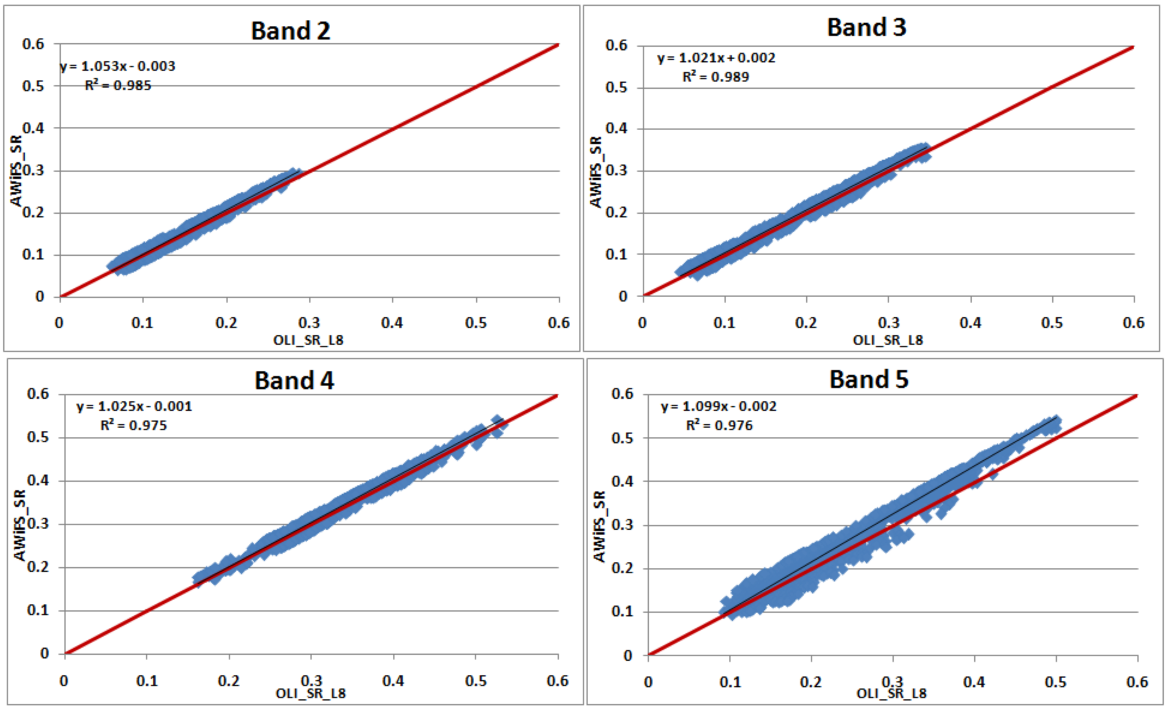


Fig.16 Scatter plot between RS2A AWiFS-C SR and OLI-L8 SR for each band DOP: 20 Feb2020

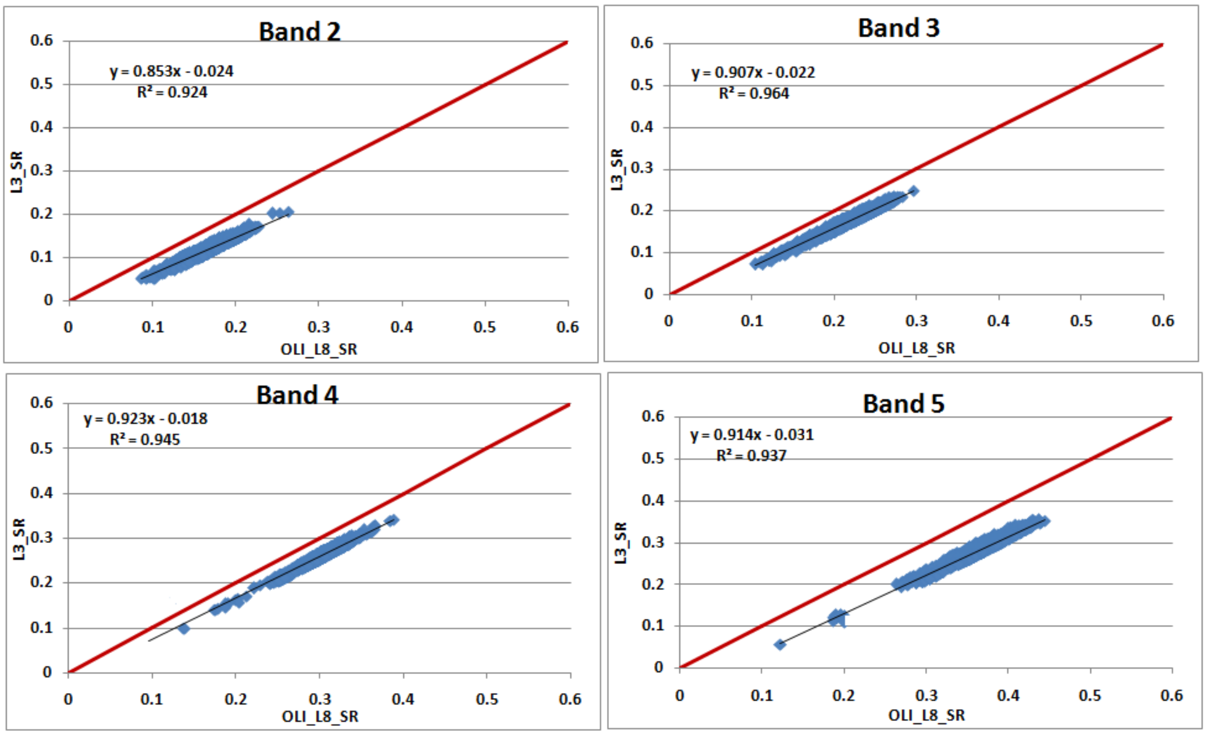


Fig.17 Scatter plot between RS2 L3 SR and OLI-L8 SR for each band DOP:22feb2020

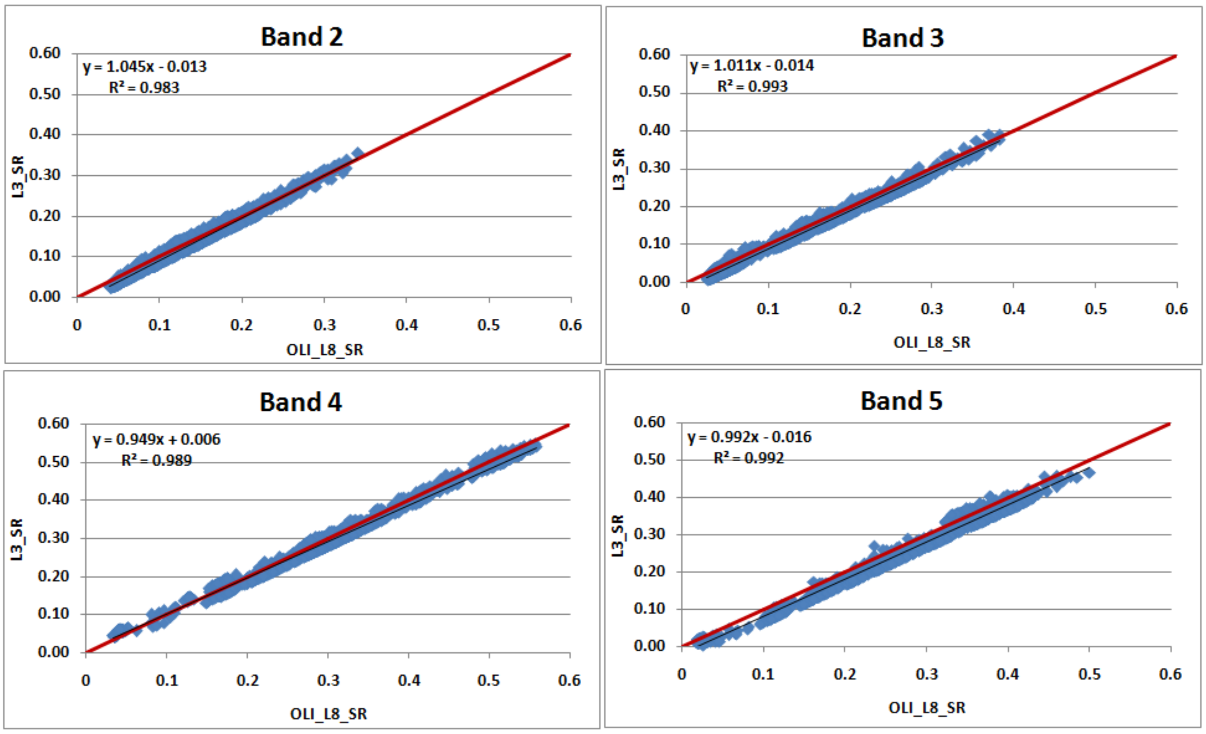


Fig.18 Scatter plot between RS2A L3 SR and OLI-L8 SR for each band DOP: 03apr2020

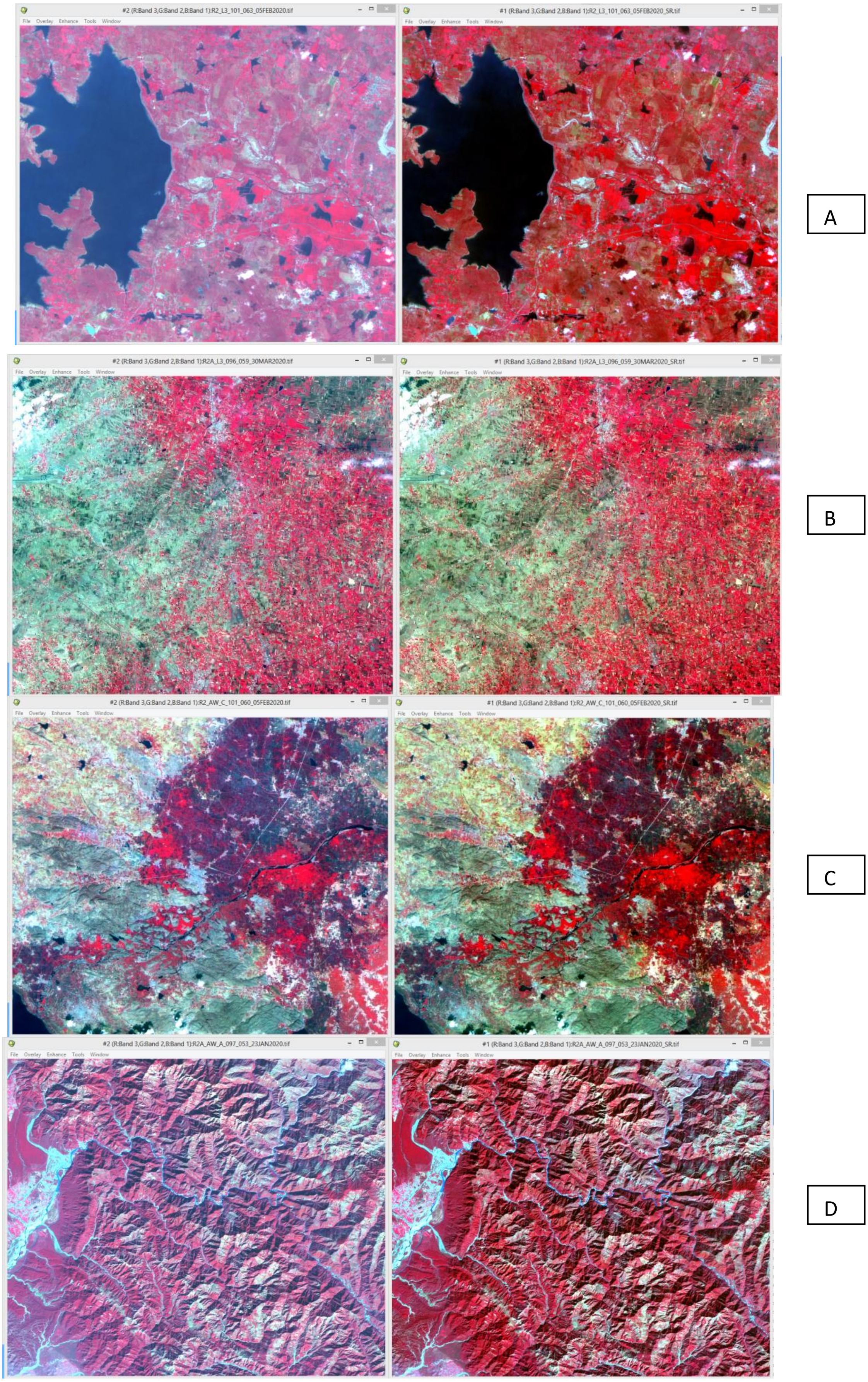


Fig.19 : (Left) DN image and SR Image (right) , A) RS2-L3 B) RS2-AWiFS C) RS2A-L3 D) RS2A AWiFS

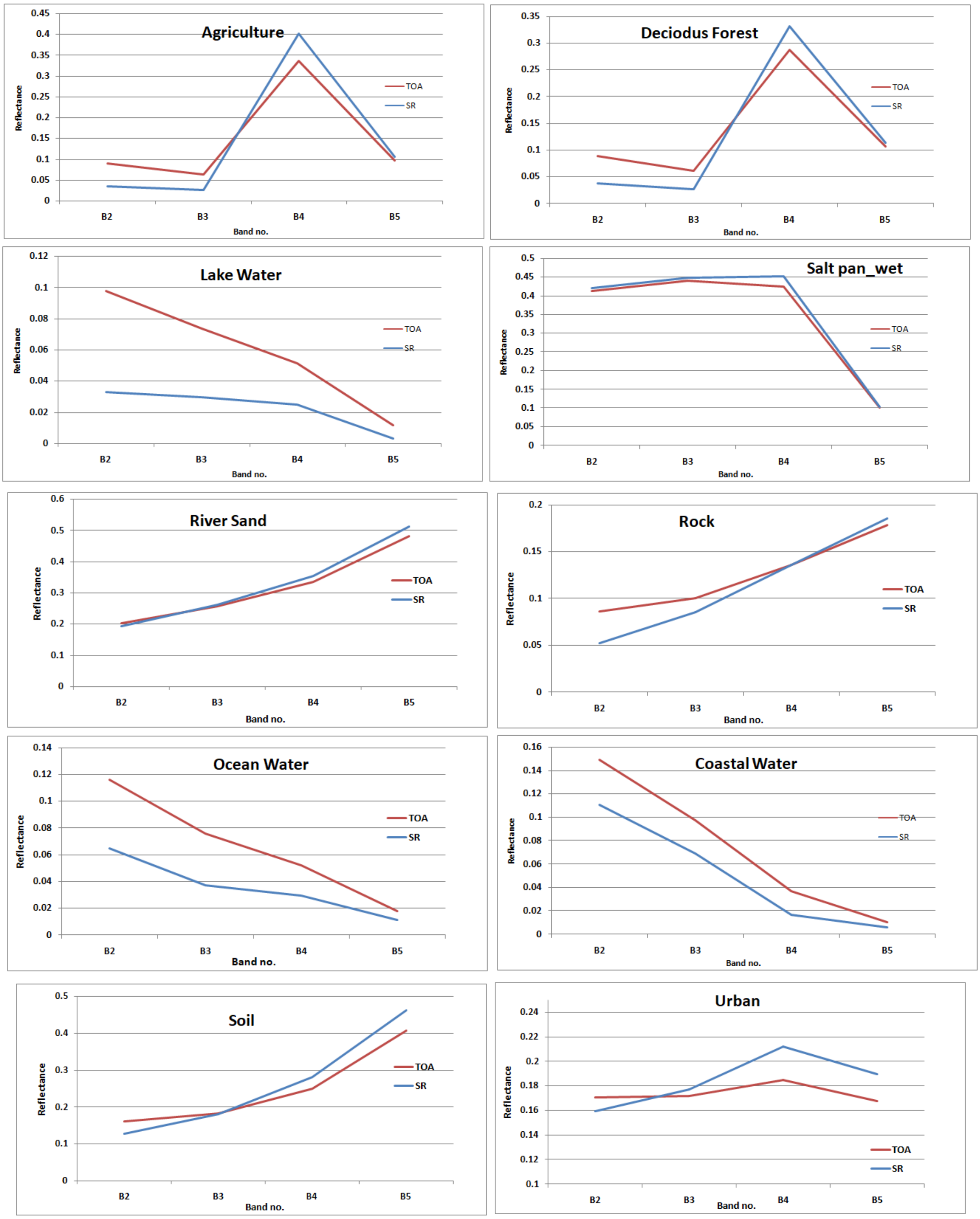


Fig.20 Results of atmospheric correction over various types of terrain features: TOA vs. Surface Reflectance

Figures 19 show the visual appearance of Atmospheric uncorrected and corrected FCC images in which haziness due the scattering effect is nullified and the contrast is increased. Spectral profiles of various terrain features before and after atmospheric correction on RS-2A L-3 image is shown in Figure 20. It is evident that scattering effect is compensated by decreasing the reflectance values in green and red bands (shorter wavelength) and absorption effects are compensated by increase in NIR and SWIR values

## 5.2Validation of Algorithm by generating surface reflectance for L8-OLI Terrain corrected products and comparing with USGS L8-OLI surface reflectance (LaSRC) products

USGS L8-OLI surface reflectance **(LaSRC: Landsat Surface Reflectance Code )**[12]products which are well calibrated and well accepted by RS community are available in the public domain for free download. These datasets are used as references to validate the accuracy of Surface reflectance from RS2 sensors. So to validate the accuracy of the algorithm, USGS L8-OLI geo-referenced data is taken and SR products were generated by running ACT module by providing necessary atmospheric data.

**Study Area/Source data**

Geo-referenced (GR) data sets of Ground areas covering full dynamic range of the sensor right from Deep Ocean, lake water to snow cover over Indian region were selected for this activity. Details are shown in Table-7. The OLI GR products are available for free downloads from https://earthexplorer.usgs.gov.

| Feature | Path-Row | DOP |
|---|---|---|
| **Desert/Barren land** | 150/41 | 28May2020 |
| | 150/42 | |
| **Vegetation/Urban/Barren land** | 143/48 | 24Mar2020 |
| | 143/49 | |
| **Snow/Ice/Hill** | 149/34 | 02Mar2020 |
| | 149/35 | |
| | 142/48 | 02Apr2020 |

Table-7: Selected OLI GR data sets

Surface reflectance was generated for first seven bands of OLI GR datasets i.e, coastal aerosol to SWIR2 bands only; as the LaSRC data is not available for Panchromatic and TIRS bands. Theoretically, minimum or no variation should exist in the values of Surface reflectance generated from ACT with respect to values of LaSRC products. Regression analysis is carried between the two data sets generated from in-house ACT s/w and LaSRC datasets.

Visual comparison is also carried out on USGS SR and in-house developed SR images by displaying them side by side with same LUT. Visual analysis shows a very good correlation between USGS and in house developed SR for all the scenes.

Regression analysis between our product with USGS generated SR was carried out for each band Separately over selected uniform targets like lake, river, snow, desert, hill, vegetation

200 X 200 pixel windows. Scatter plots for the same are shown in Fig-21 to Fig-28. Mixture targets were also selected and used for regression. Results are depicted in Fig-27 to Fig-28. Reference USGS SR band is selected as X-Axis against which in-house developed SR band is plotted as Y-axis.

For each feature, slope and offset values of ACT- SR images with respect to LaSRC are tabulated and shown in the same figure. Slopes are close 1 and offsets are close to zero for the bands B2 to B7. Variation is more in B1 , the band which is sensitive to Aerosols and especially deviation is more on low reflectance features in that wavelength band like water bodies and vegetation. Good agreement is seen for this band on the high reflectance features.

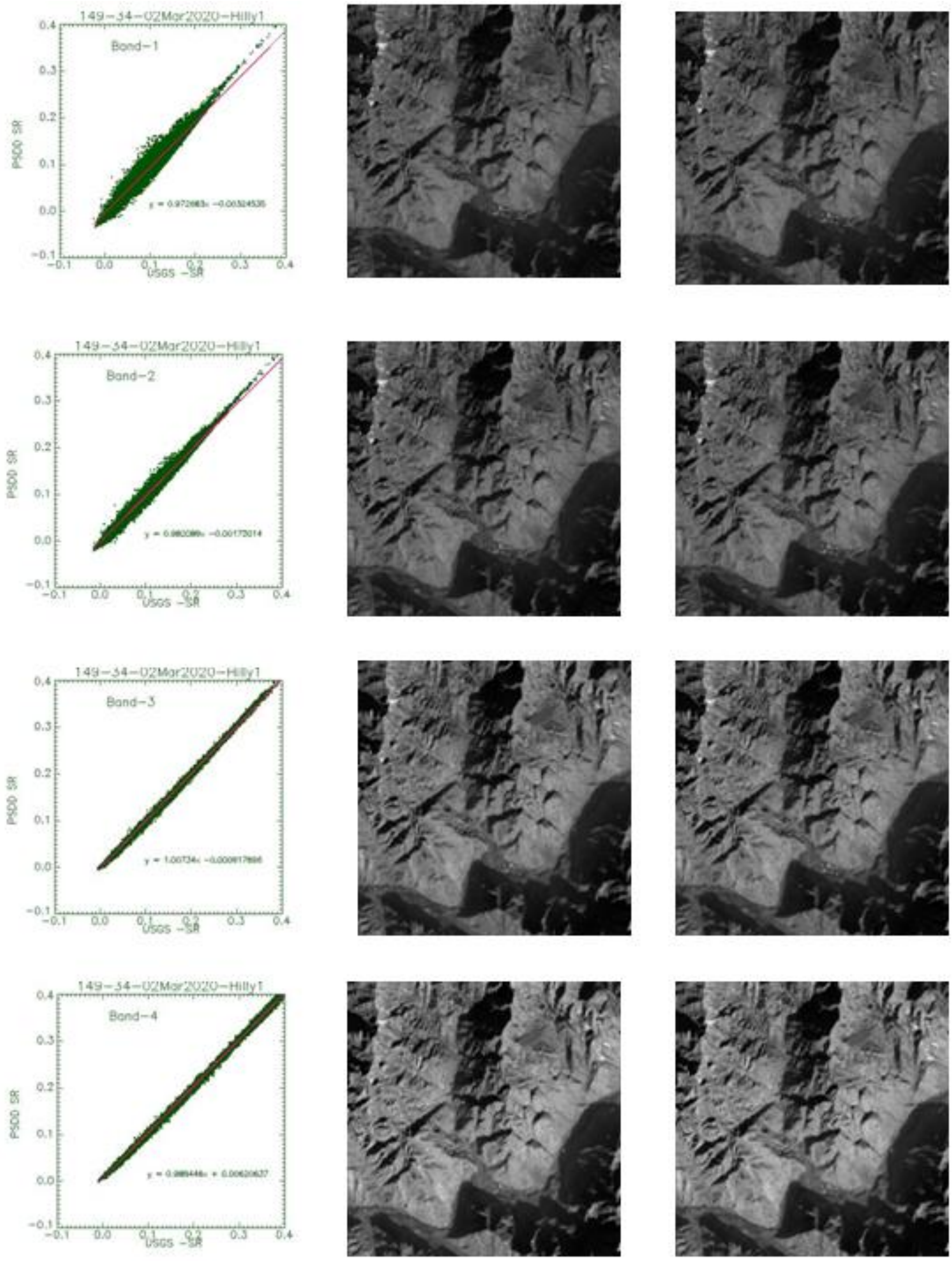

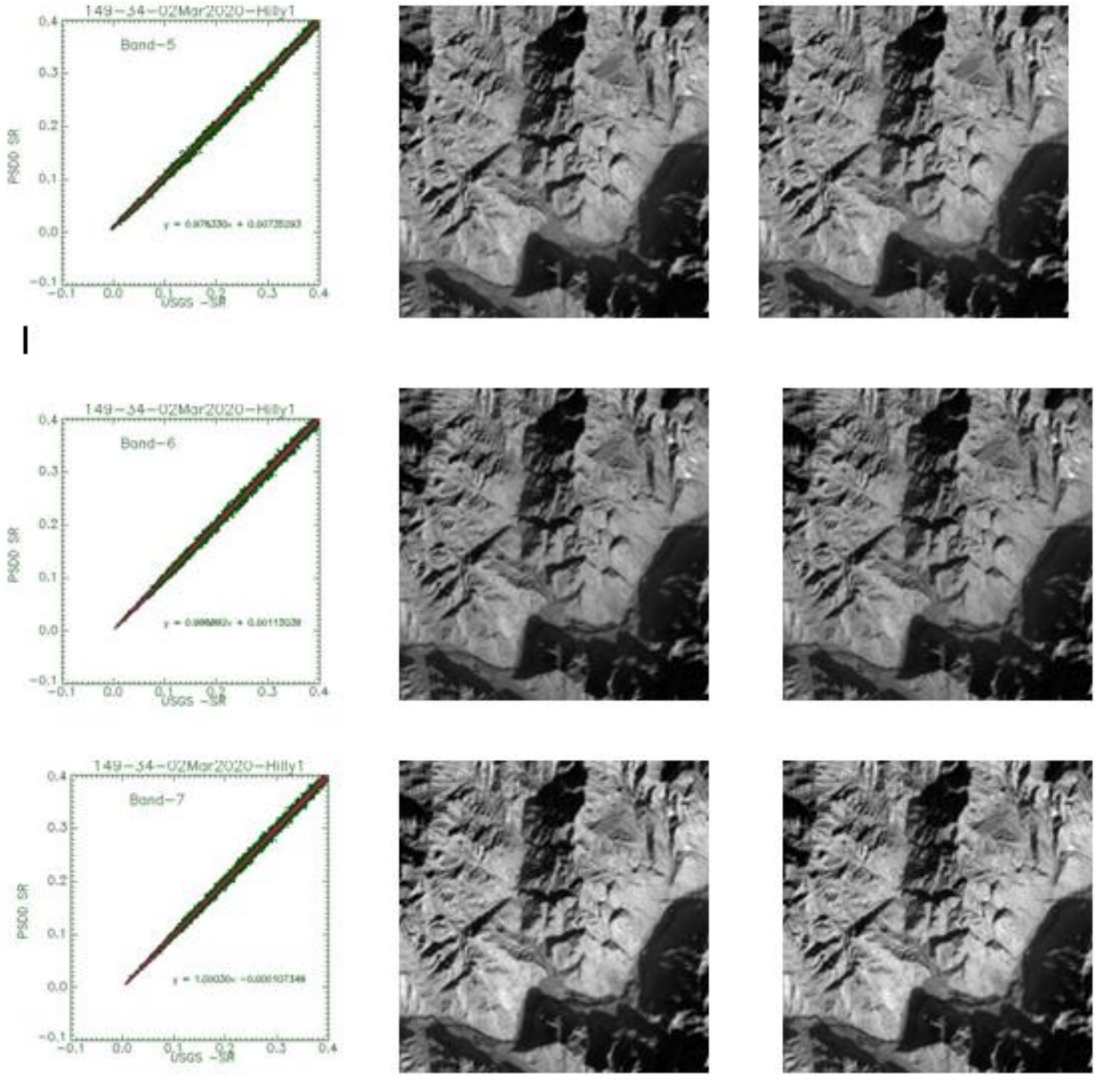


Fig21149/34 , 02MAR2020, Target : Hilly USGS SR ACT SR

| Target : Hill Rocky<br>Band no | Slope | Offset |
|---|---|---|
| 1 | 0.973 | -0.003 |
| 2 | 0.982 | -0.001 |
| 3 | 1.007 | -0.001 |
| 4 | 0.988 | 0.006 |
| 5 | 0.978 | 0.007 |
| 6 | 0.999 | 0.001 |
| 7 | 1.0003 | -0.0001 |

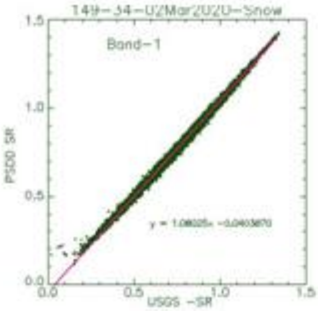
149-34-02Mar2020-Snow
Band-1
PSDD SR
USGS -SR
0.0
0.5
1.0
1.5
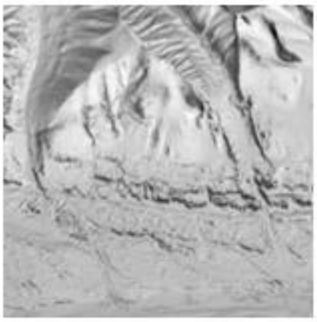

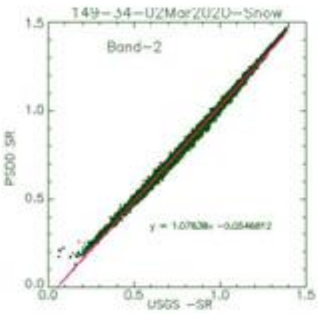
149-34-02Mar2020-Snow
Band-2
PSDD SR
USGS -SR
0.0
0.5
1.0
1.5
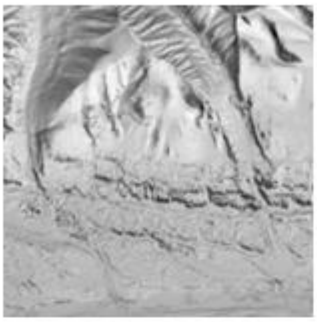
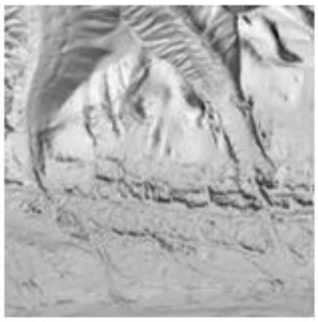
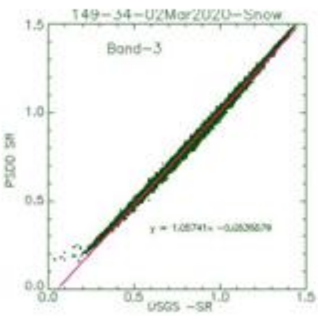
149-34-02Mar2020-Snow
Band-3
PSDD SR
USGS -SR
0.0
0.5
1.0
1.5
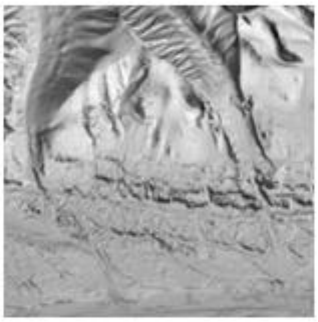

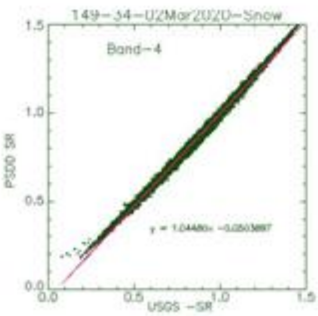
149-34-02Mar2020-Snow
Band-4
PSDD SR
USGS -SR
0.0
0.5
1.0
1.5

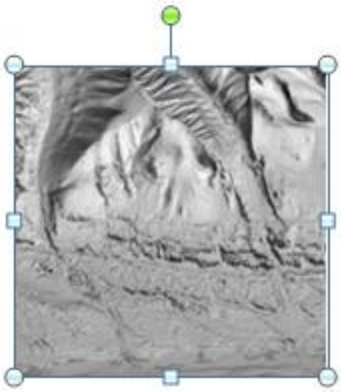

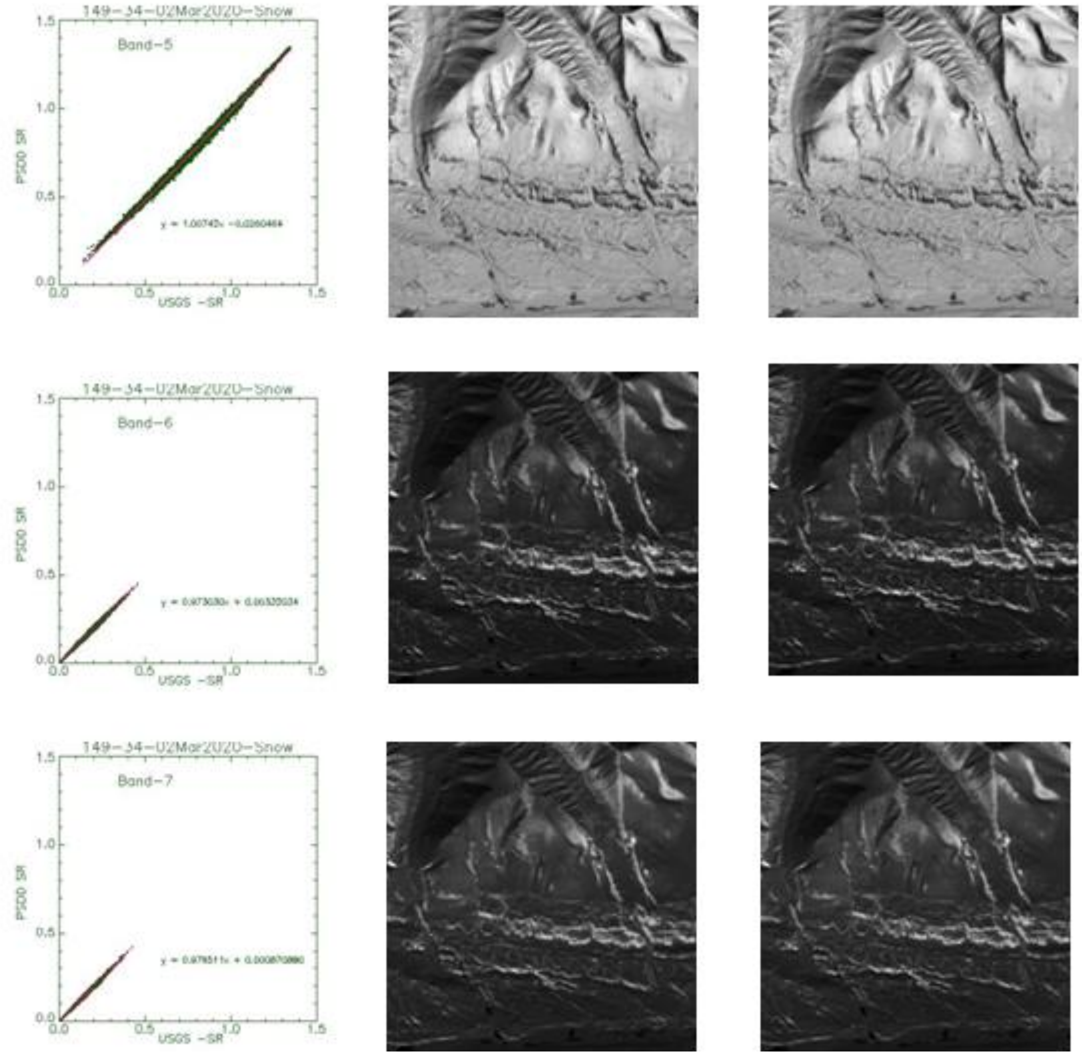


**Fig.22**149/34 , 02MAR2020, Target : SNOW USGS SR ACT SR

| Target : Snow<br>Band no | Slope | Offset |
|---|---|---|
| 1 | 1.080 | -0.4003 |
| 2 | 1.078 | -0.054 |
| 3 | 1.057 | -0.053 |
| 4 | 1.044 | -0.050 |
| 5 | 1.007 | -0.026 |
| 6 | 0.9730 | 0.003 |
| 7 | 0.9795 | 0.0008 |

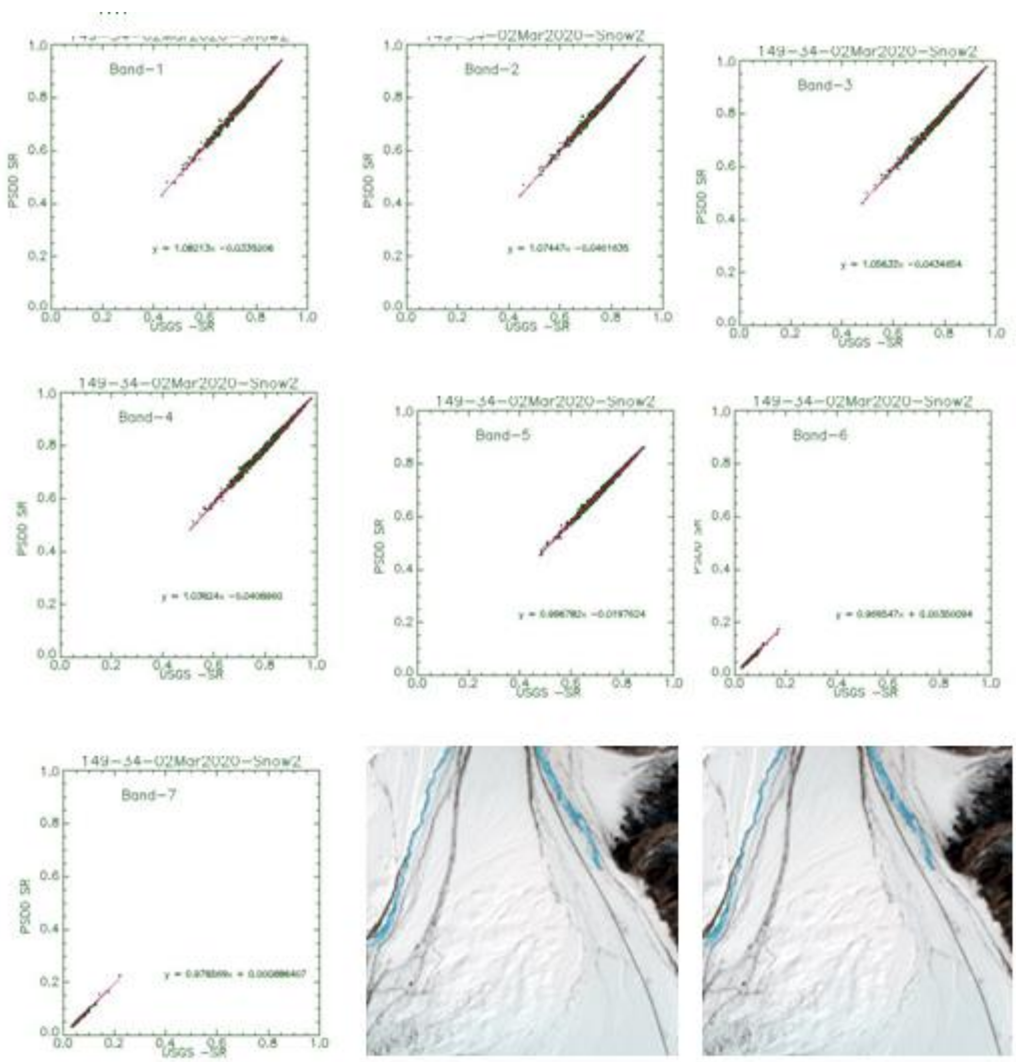


USGS-SR In house developed -SR

| Target : Snow<br>Band no | Slope | Offset |
|---|---|---|
| 1 | 1.082 | -0.033 |
| 2 | 1.074 | -0.046 |
| 3 | 1.056 | -0.043 |
| 4 | 1.0138 | -0.040 |
| 5 | 0.9967 | -0.019 |
| 6 | 0.9695 | 0.0035 |
| 7 | 0.9785 | 0.0008 |

Fig.23 149/34 , 02MAR2020, Target : LAND+SNOW

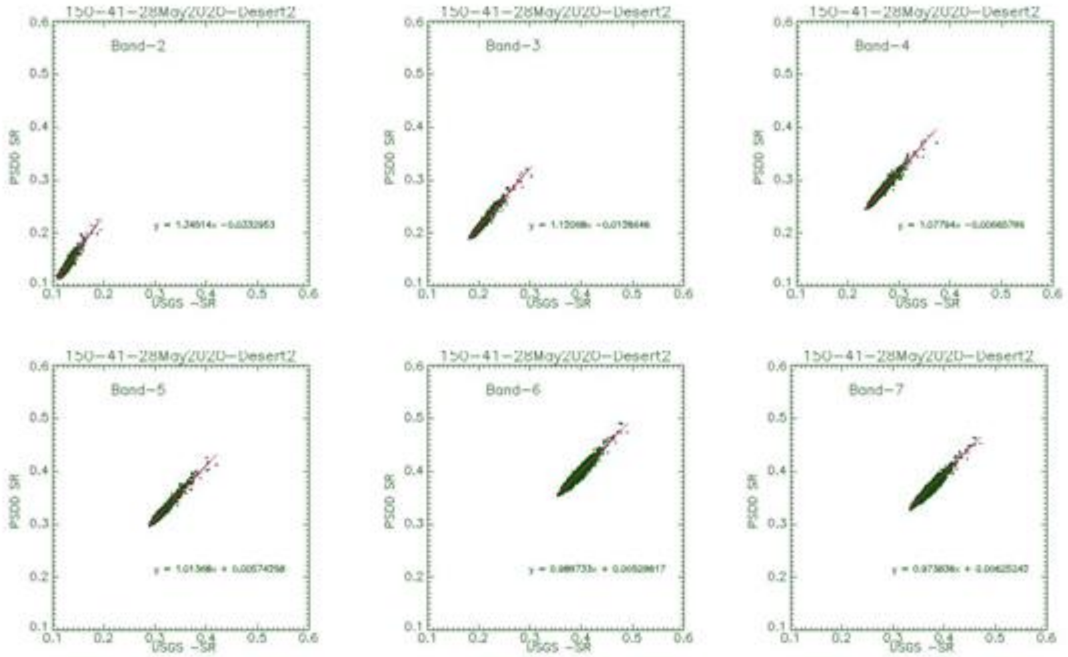


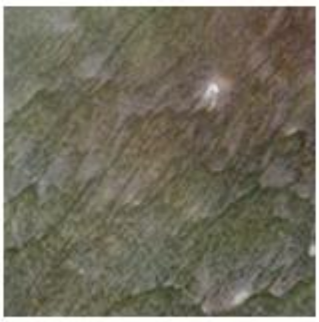

USGS-SR

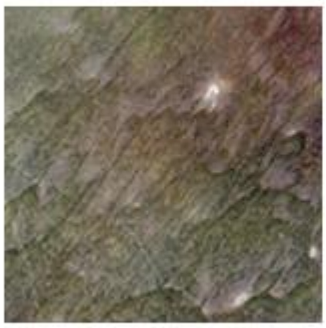

In house developed -SR

| Target : Snow<br>Band no | Slope | Offset |
|---|---|---|
| 1 | 1.362 | -0.056 |
| 2 | 1.345 | -0.033 |
| 3 | 1.120 | -0.013 |
| 4 | 1.077 | -0.006 |
| 5 | 1.0136 | 0.005 |
| 6 | 0.9897 | 0.005 |
| 7 | 0.9738 | 0.006 |

Fig-24 :150/41 , 28May2020, Target : Desert

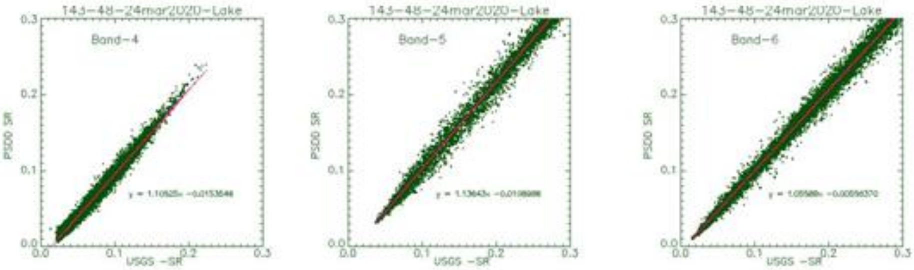


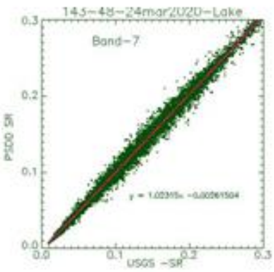


| Target : Snow Band no | Slope | Offset |
|---|---|---|
| 1 | 0.645 | 0.0009 |
| 2 | 0.851 | -0.0097 |
| 3 | 1.105 | -0.0197 |
| 4 | 1.1052 | -0.0153 |
| 5 | 1.1364 | -0.0108 |
| 6 | 1.055 | -0.005 |
| 7 | 1.023 | -0.0026 |

Fig-25 :143/48 , 24mar2020 , Target : lake : Low aerosol variation: 0.3 to 0.7

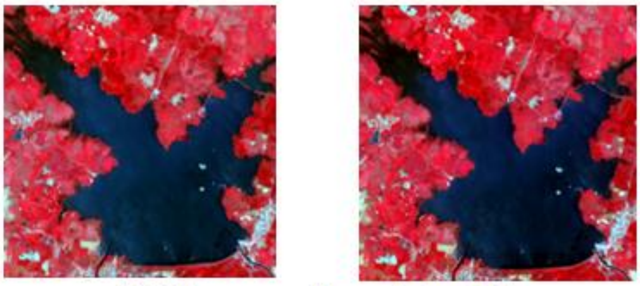

USGS-SR In house developed -SR

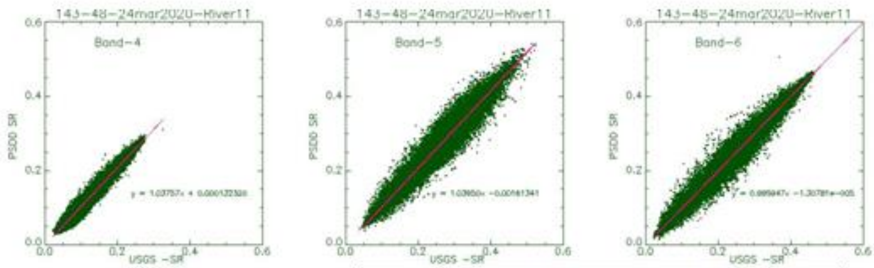


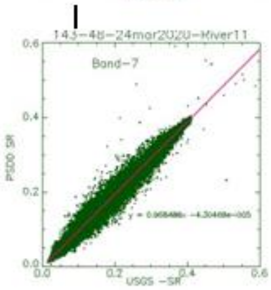


| Target : River+Vegetation Band no | Slope | Offset |
|---|---|---|
| 1 | 0.911 | 0.026 |
| 2 | 0.9807 | 0.0119 |
| 3 | 1.0511 | -0.0009 |
| 4 | 1.037 | 0.0001 |
| 5 | 1.039 | -0.001 |
| 6 | 0.9959 | -0.0001 |
| 7 | 0.9684 | -0.0004 |

Fig-26 :143/48 , 24mar2020 , Target : River, Vegetation : Low AOD variation: 0.3 to 0.7

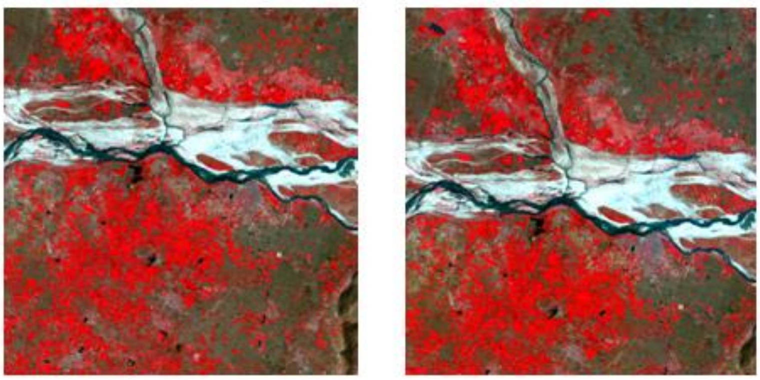

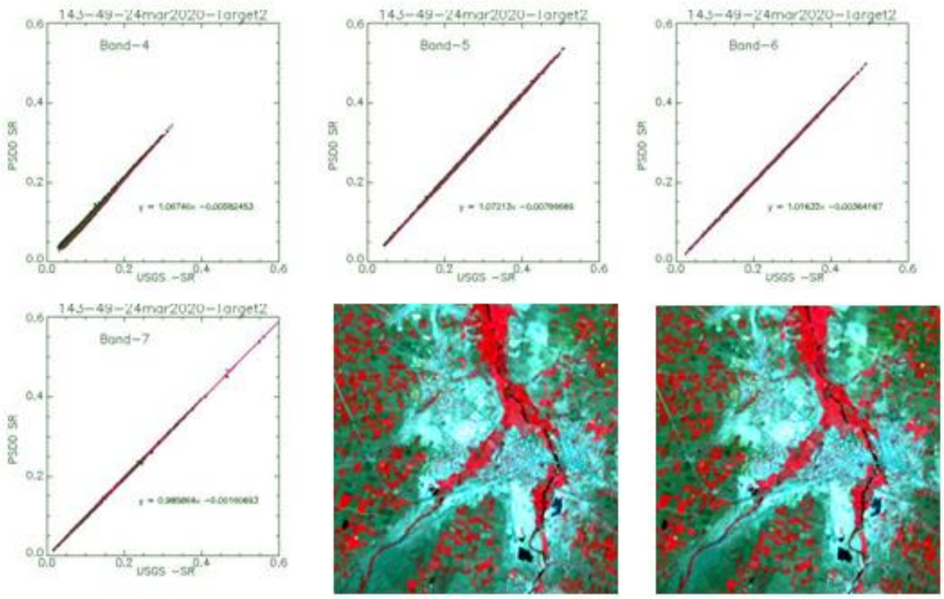


USGS-SR

In house developed -SR

| Target : Urban Band no | Slope | Offset |
|---|---|---|
| 1 | 1.0253 | 0.0111 |
| 2 | 1.1022 | -0.0025 |
| 3 | 1.122 | -0.0116 |
| 4 | 1.0674 | -0.0058 |
| 5 | 1.0721 | -0.0079 |
| 6 | 1.0163 | -0.0036 |
| 7 | 0.9858 | -0.0016 |

Fig-27: 143/49 , 24mar2020, Target : Urban, Low AOD variation: 0.04 to 0.4

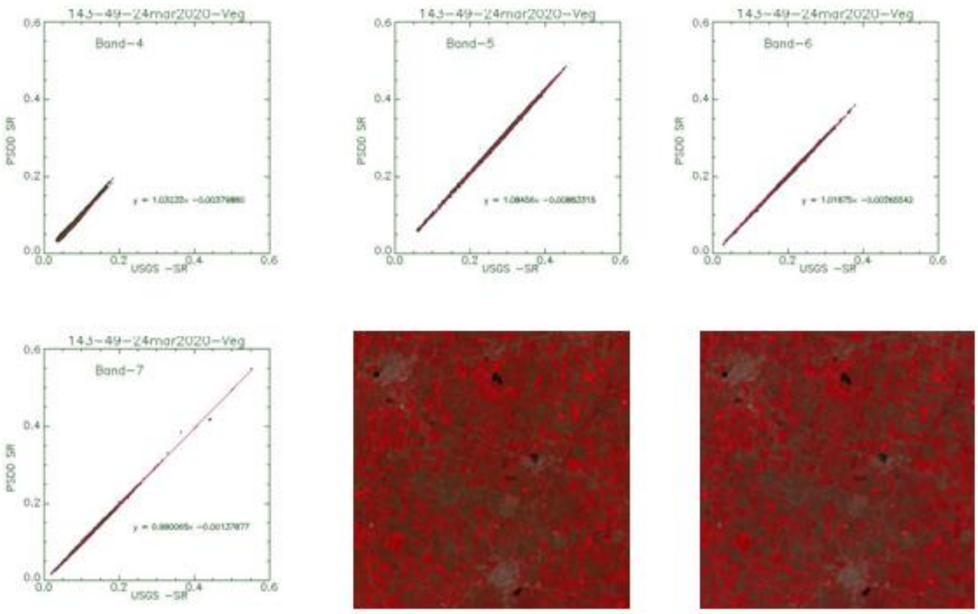


USGS-SR

In house developed -SR

| Target : Vegetation Band no | Slope | Offset |
|---|---|---|
| 1 | 0.830 | 0.015 |
| 2 | 0.945 | 0.002 |
| 3 | 1.042 | -0.006 |
| 4 | 1.032 | -0.003 |
| 5 | 1.084 | -0.008 |
| 6 | 1.018 | -0.002 |
| 7 | 0.9900 | -0.001 |

Fig-28 : 143/49 , 24mar2020 , Target : VEGETATION : Low AOD variation: 0.04 to 0.4

In-house ACT Software was developed to realize surface reflectance from geo-reference data of Landsat-8 OLI bands B1 to B7. A good agreement was observed between the in-house developed SR and USGS SR(LaSRC) for the bands 1 to 7 of Landsat-8 OLI. This analysis also proves the methodology/algorithm developed to generate the surface reflectance from radiance images. Deviation is little bit more in shorter wavelength bands which are sensitive to the atmospheric aerosol type and concentrations especially over low reflectance features. This can also be attributed to the fact that to generate Landsat-8 USGS SR generation algorithm derives the AOD from the image itself and is not available to the public domain, whereas ACT SR algorithm uses INSAT /MODIS AOD values. Variation between these values might lead to differences in the SR values.

## 5.3 Validation with In-situ measurements on Latest datasets

The accuracy of the ACT algorithm was validated on RS-2A AWiFS datasets using ground radiometric measurements over uniform snow (Gulmarg,Srinagar) and desert (Lanela, Rajasthan) [13-14] sites carried out by cal-val Team as part of their vicarious calibration campaign. The SR Values at different locations were compared with spectro-radiometer measured values after convolving with RSR of the sensor. The relative differences were computed and the average value of relative difference is displayed in Table 8 below for both the scenes evaluated.

Relative Diff= (Spectro-radiometer Reflectance - ACT Reflectance) *100/Spectro-radiometer Reflectance

| | **Relative Diff (in %) wrt Ground measurement: RS-2A/AWiFS** | | | |
|---|---|---|---|---|
| | (Snow) 19-Feb-21 With Atm. Data from MODIS | (Snow) 19-Feb-21 With Atm. Data from ground measurements | (Snow)19-Feb-21 With Atm. Data from ground measurements + After removing sensor calibration error of 12 % | (Desert Sand) 24-Mar-21 |
| **B2** | 24.27 | 18.08 | **6.08** | **-2.57** |
| **B3** | 21.28 | 15.79 | **3.79** | **-2.24** |
| **B4** | 19.02 | 14.35 | **2.35** | **-1.65** |
| **B5** | NA | NA | **NA** | **-2.17** |

Table-8: ACT – SR vs. Ground measurements

ACT generated SR values are in very good agreement with ground measured values on desert targets where as more deviation is observed in case of high reflectance snow target.

Around 20% relative difference is observed wrt to ground measurement when AOD, WV& Ozone values are taken from MODIS data (0.03, 1.14 & 257.7).whereas the differences have come down to 15% when AOD, WV& Ozone values are taken from ground measured instruments (0.2, 1.7 & 334).However, it is published from the CALVAL-team [13-14] that the sensor contribution itself is about 12% error over Snow target on that day. Hence, after removing the sensor calibration error of 12%, ACT SR values are close to ground measurements within 5%.

It is also observed that sensor performance is non-linear in both very low (clear water) and very high (snow) reflectance regions and the SR deviation is also found more.

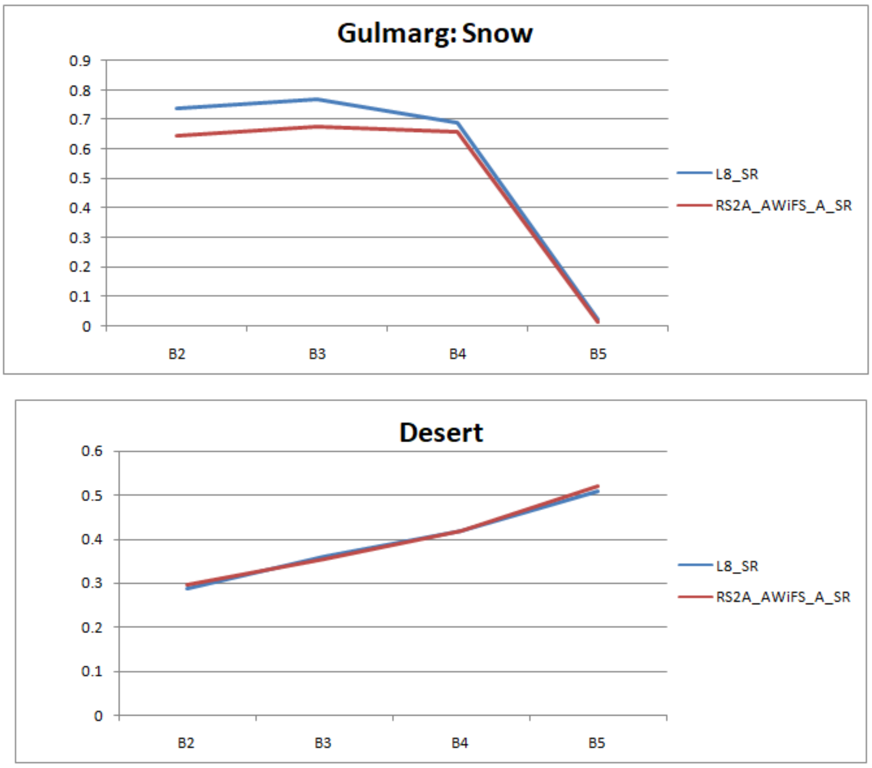


Fig-29 : ACT SR vs. L8-OLI-SR over Calibration sites

A parallel comparison in SR values over the calibration sites is also carried out wrt L8-OLI-LaSRC. Results are shown in Fig-29.

It is evident that even L8-OLI LaSRC values are also having more deviation over the high reflectance regions. Moreover, it should be kept in mind that L8-OLI LaSRC uses its own sources of Atmospheric data which causes the deviation in some cases.

### 5.4 Analysis on temporal consistency

To evaluate the robustness/ stability/ temporal consistency of the algorithm, two areas over which temporal variation of AOD exists are considered. Areas are chosen in such a way that AOD values are more due to anthropogenic process like coal burning in NTPC-Vindhyachal and agricultural wastage burning near Delhi. Details of the datasets are given in Table 9. Theoretically, minimum or no variation should exist in surface reflectance of the pseudo invariant targets though the atmospheric conditions might vary drastically.

| Area | Sensor: R2A-L3 Path/Row,DOP | Sensor: L8- OLI Path/Row, DOP | MODIS AOD Value |
|---|---|---|---|
| NTPC- Vindhyachal | 102/55 01-Dec-2020 | 142/43 28-Nov-2020 | **0.3976** |
| | 102/55 07-Mar-2021 | 142/43 04-Mar-2021 | **0.1966** |
| Delhi | 96/51 19-Dec-2020 | 146/40 26-Dec-2020 | **0.26** |
| | 96/51 01-Mar-2021 | 146/40 28-Feb-2021 | **0.43** |

Table-9: Selected data sets to check temporal consistency

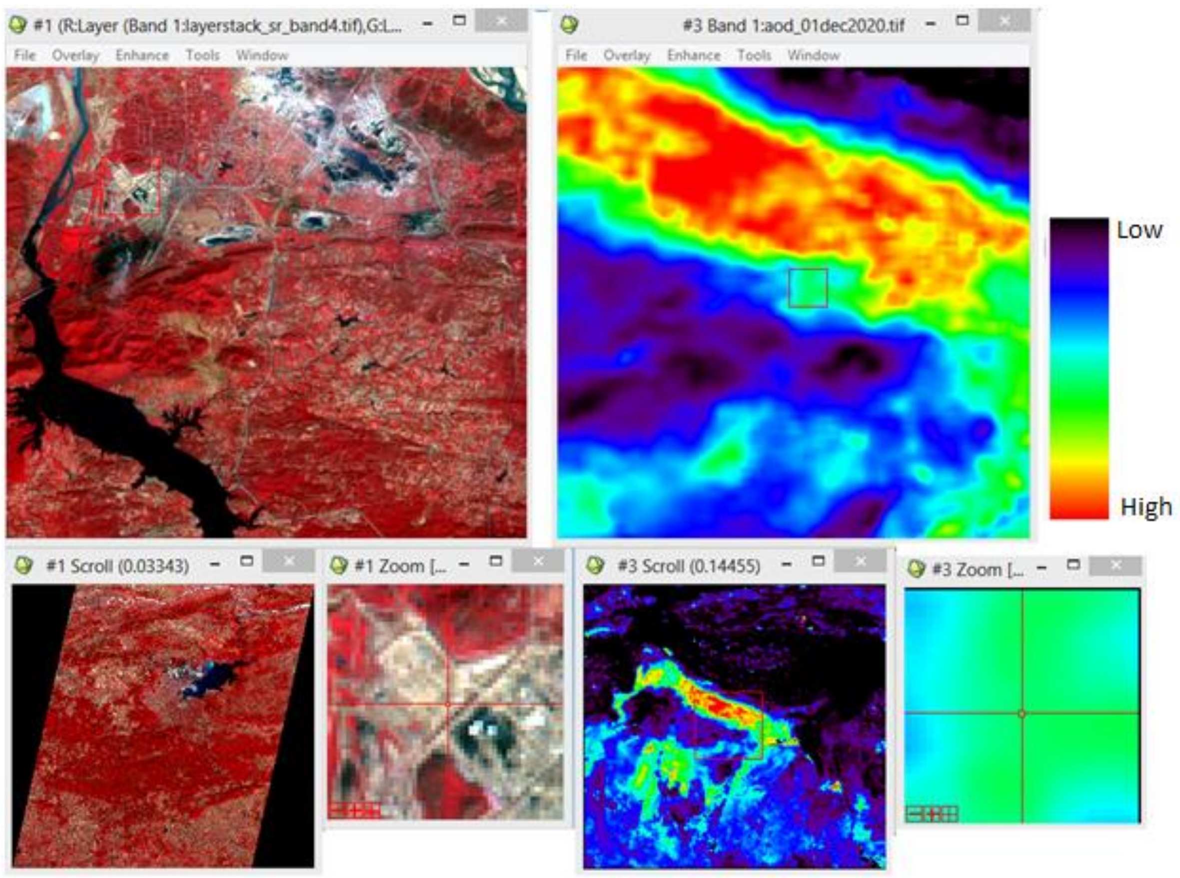


Fig-30 : Left: NTPC Vindhyachal: R2A-L3: 102/55, 01-Dec-2020
Right: MODIS AOD 01-Dec-2020: value **0.3976**

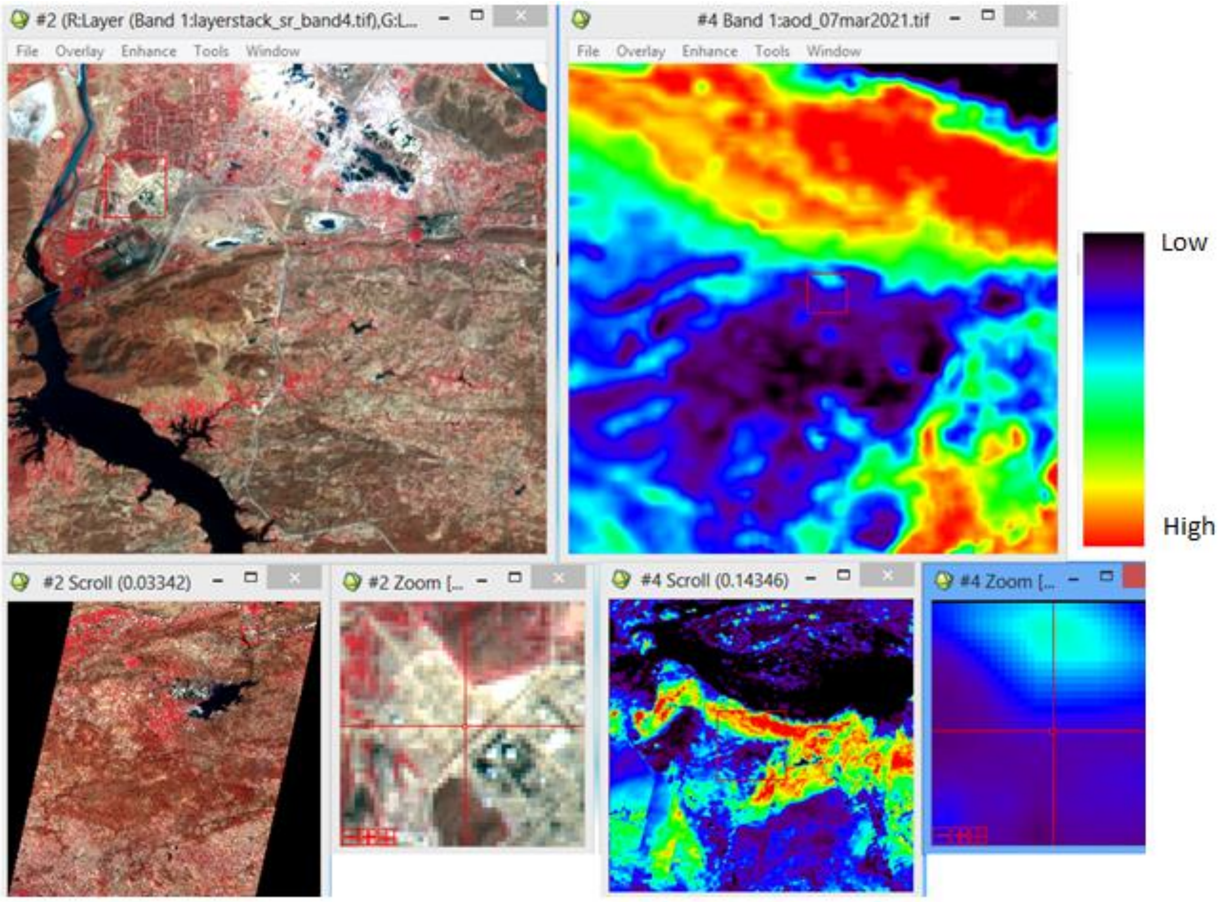


Fig-31: Left: NTPC Vindhyachal: R2A-L3: 102/55, 07-Mar-2021
Right: MODIS AOD 07-Mar-2021: value **0.1966**

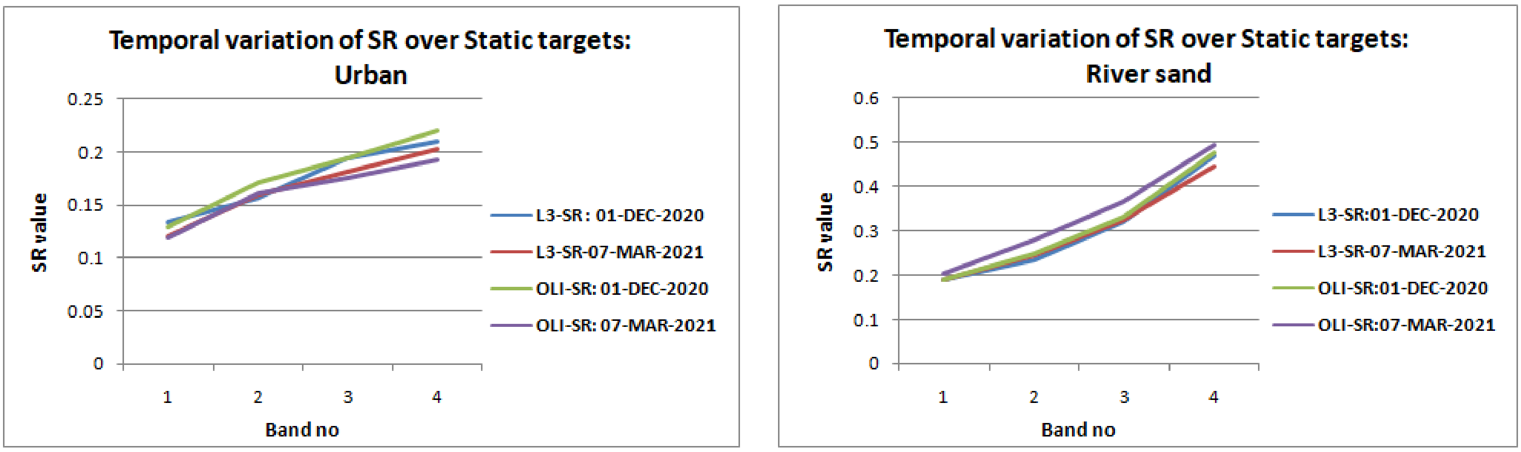


Fig-32: Temporal variation of SR over static targets like urban and River sand: NTPC

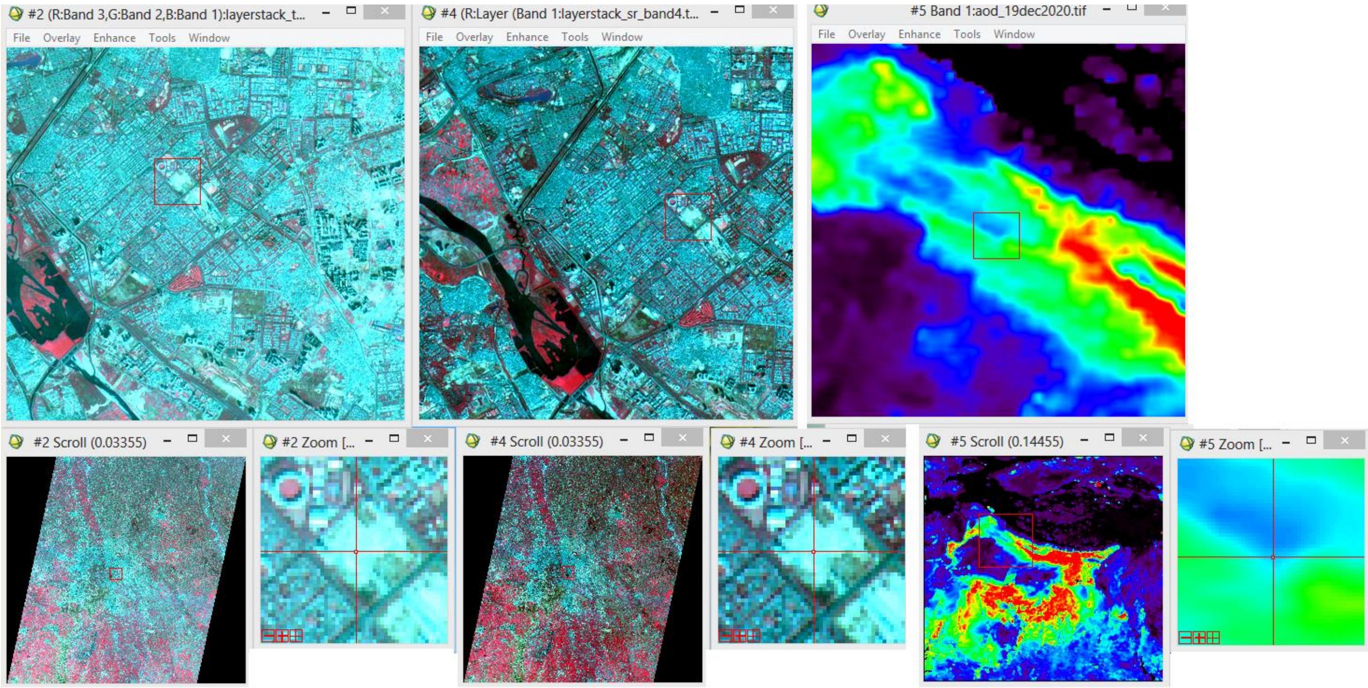


Fig-33. Delhi: R2A-L3:96/51, 19-Dec-2020, : Left: TOA, Middle: SR
Right: MODIS AOD 19-Dec-2020: value **0.26**

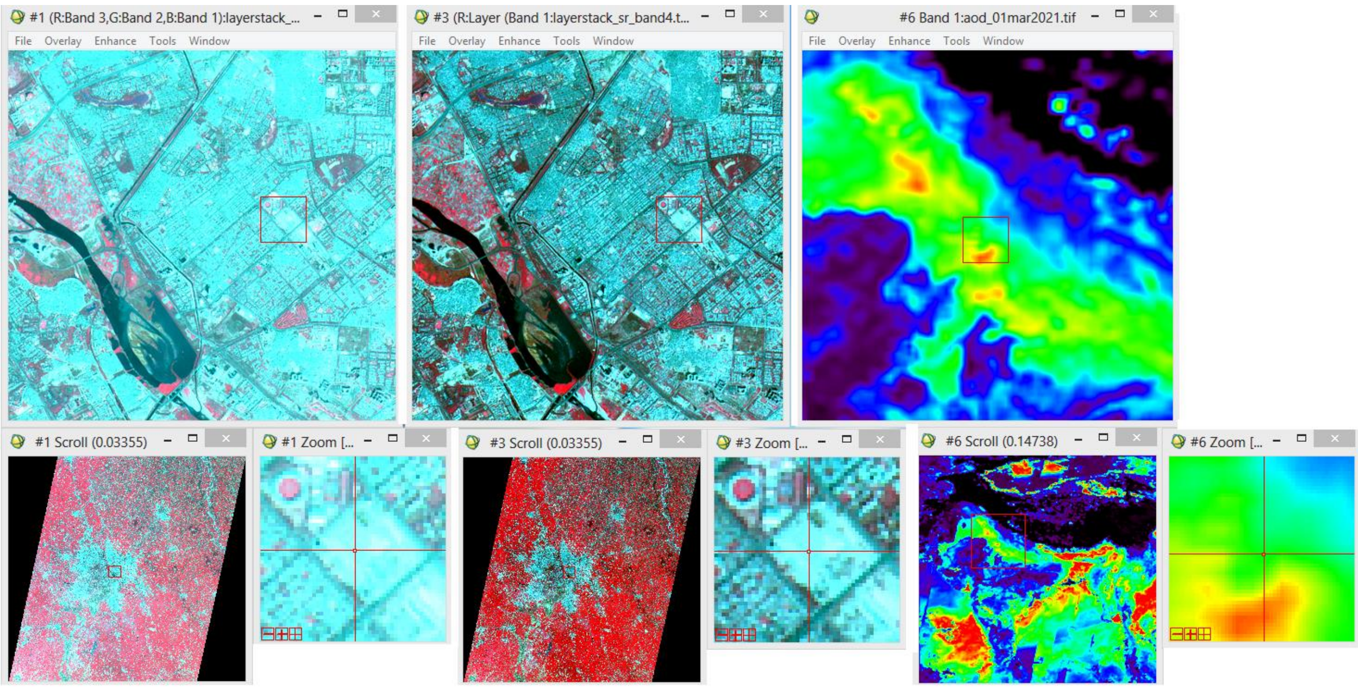


Fig-34: Delhi: R2A-L3:96/51, 01-Mar-2021, Left: TOA, Middle: SR
Right: MODIS AOD 19-Dec-2020: value **0.43**

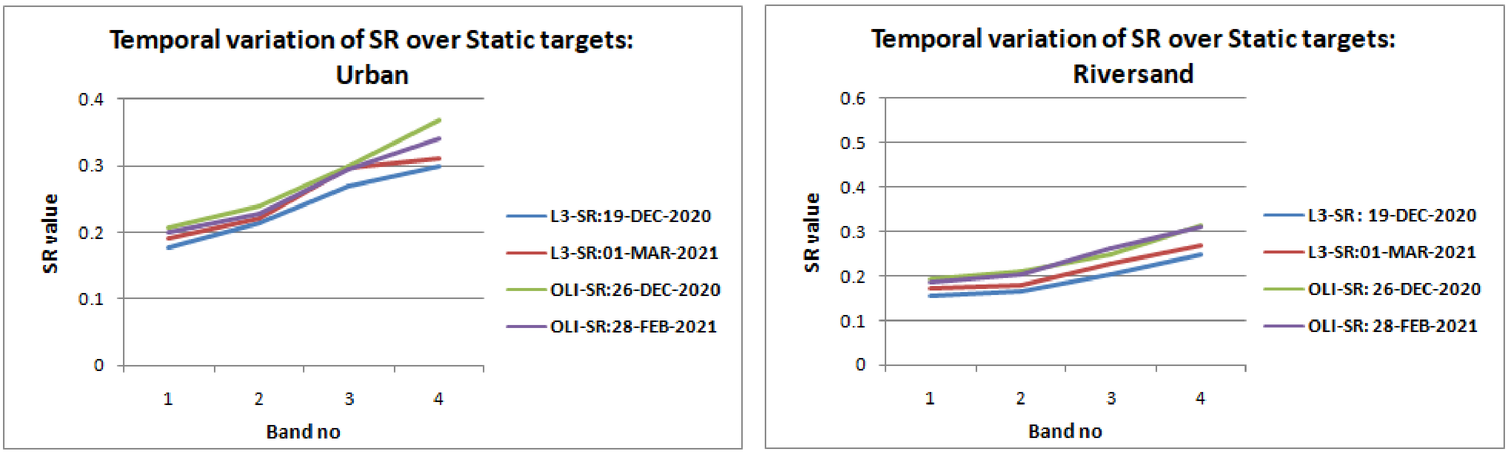


Fig-35: Temporal variation of SR over static targets like urban and River sand: Delhi

Fig-30 and Fig-31 shows the FCC images of NTPC-Vindhyachal area of 19dec2020 and 01Mar2021. AOD variation from the MODIS is increased from 0.19 to 0.39 which is almost double. SR values of these areas for both the dates are computed and plotted for pseudo invariant targets like urban and River sand in Fig-32. It can be seen that though the atmosphere is contaminated with Varied AOD, SR values variation from ACT s/w is found less than 5 %. It is observed that OLI-L8-LaSRC also following the same trend of less than 5 % variation.

Similar trend was also observed over Delhi area which is shown in Fig-33, Fig-34 and Fig-35. In this case, AOD variation from 19Dec2020 to 01Mar2021 is 0.26 to 0.43 and SR variation between these dates is still within 5%.

This analysis further confirms the stability of the algorithm for various values of input combinations.

### 5.5 Results after topographic correction

Satellite imagery in mountainous terrain is affected due to sharp variations in the topographic parameters such as altitude, slope and aspect. The topographic variability causes a problem of differential illumination due to steep and varying slopes as in rugged Himalayan terrain. Sun facing illuminated slopes (south aspect) show more than expected radiance or reflectance, whereas the effect is opposite in shadowed regions (north aspect). Therefore a topographic correction which compensates the problem of differential solar illumination is essential for qualitative and quantitative analysis of snow cover applications.

To analyse and compare the spectral reflectance over Himalayan regions, RS2/AWiFS images were subjected to topographic corrections. The topographic corrections are realized using slope matching techniques [15] which is reported to be most suitable for Himalayan terrain.

Comparative analysis is also carried out with Landsat-8/OLI surface reflectances over same targets. Details of the datasets of are given below.

| **Area** | **Sensor, path/row, DOP,AOD** | **L8- OLI details** |
| --- | --- | --- |
| Himalayas | R2-AWiFS, 99/48<br>03-Dec-2020 | OLI-L8 147/38<br>01-Dec-2020 |

Table-10: Selected data sets for topographic correction

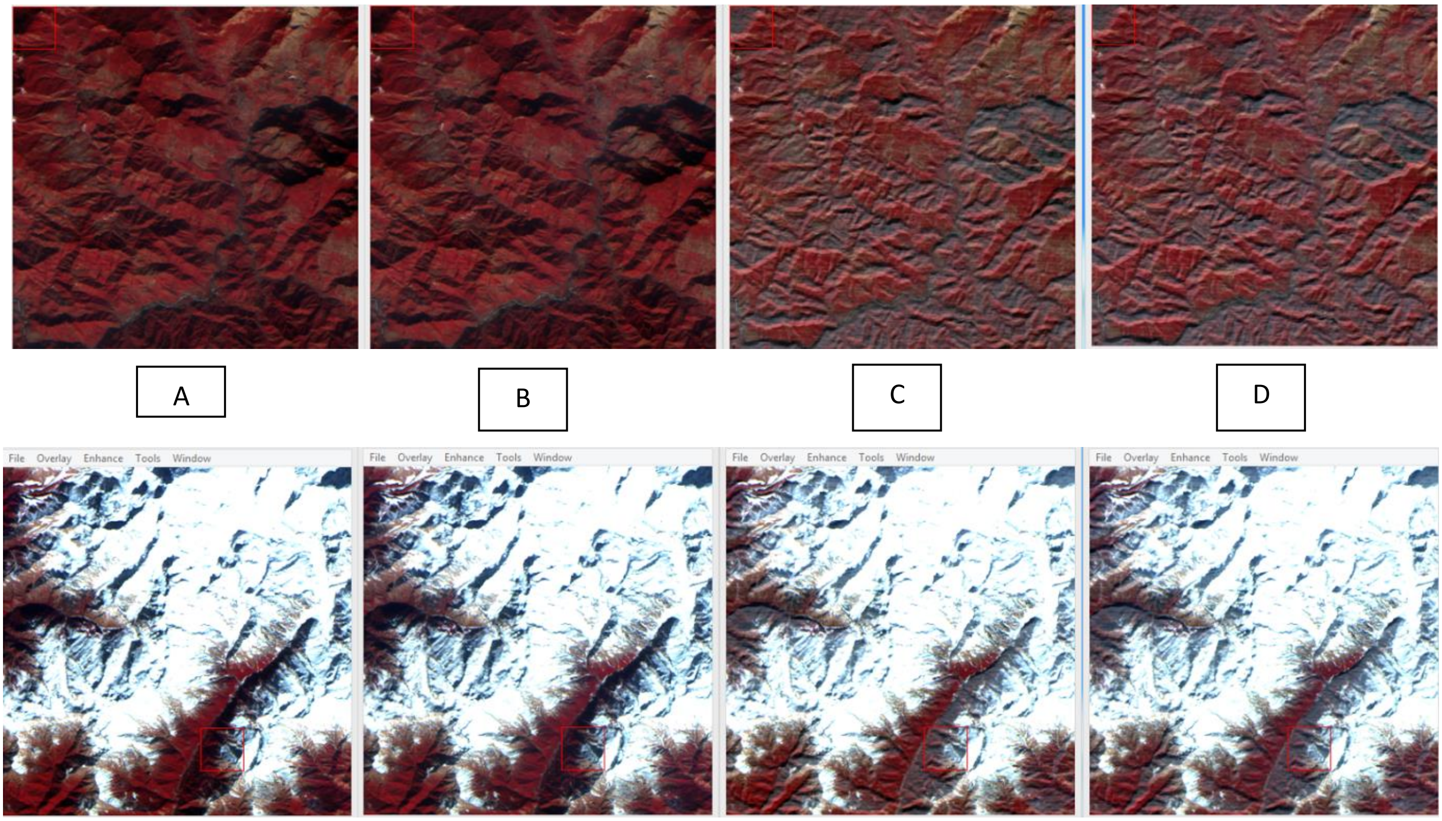


Fig-36: A - TOA before Topographic Correction: C - TOA after Topographic Correction
B - SR before Topographic Correction: D - SR after Topographic Correction

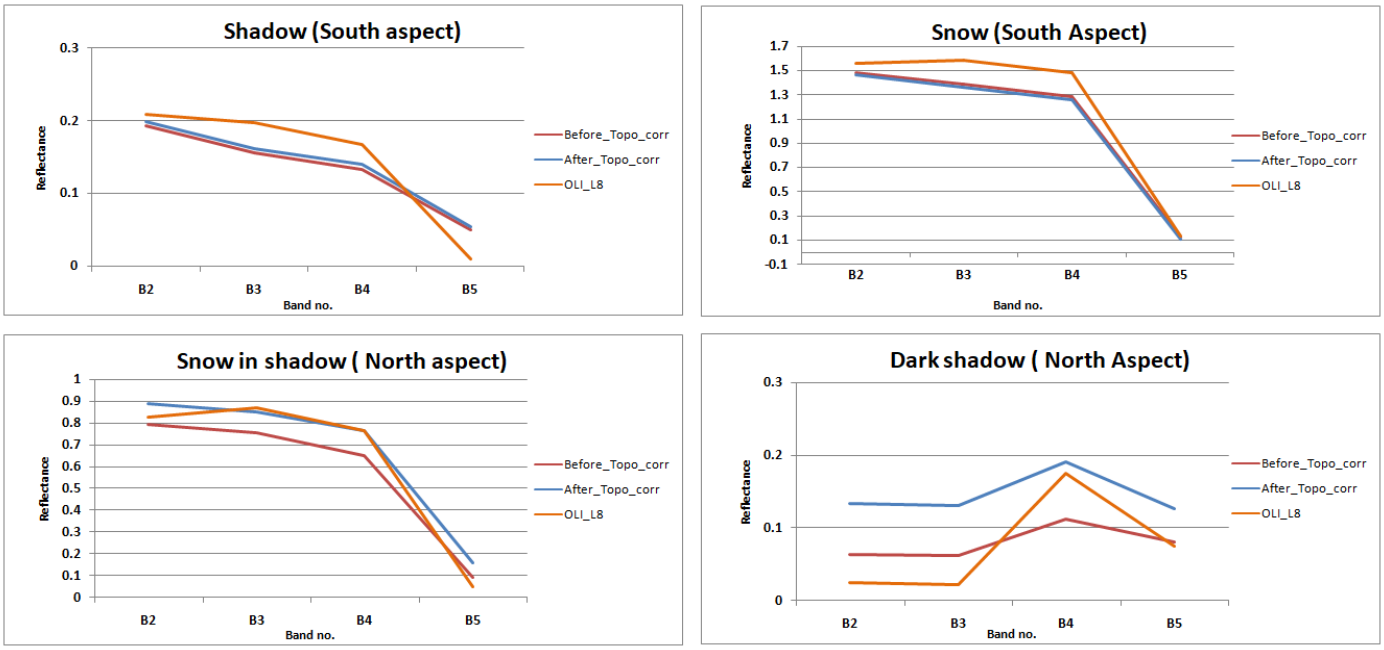


Fig-37 : Effects Of Topographic Correction

Fig-36 shows how the topographic correction compensates the differential illumination effects over highly undulated terrains like Himalayas. From both TOA and SR images, it is obvious that reflectances are significantly improved in north aspect shadowed regions. Whereas permanent illuminated south aspect images are kept intact. A comparative analysis is also carried out wrt to L8-OLI-LaSRC images and the results are shown in Fig-37.

In general, L8-SR values aremore over high reflectance targets like snow compare to RS-2/2A SR values in both illuminated and shadowed regions. Whereas after topographic correction, RS2/2A SR values over shadowed regions are matching with L8-SR values which clearly indicates that L8-OLI LaSRC algorithm is not carrying out the topographic correction.

# 6. Limitations

The use of a Lambertian surface approximation instead of bi-directional reflectance distribution function (BRDF) can deteriorate the accuracy in the backscattering direction. Also, the uncertainties associated with atmospheric products derived from MODIS atmospheric products directly affect the accuracy of surface reflectance products.

AOD data from MODIS has voids over Himalayan terrain most of the times. Using either a constant value or extrapolation from available neighbourhood pixels may affect the accuracy over those regions. Accuracy of surface reflectance of water pixels is to be further validated especially for LISS-3 sensor.

# 7. Conclusion

The per-pixel atmospheric correction method employed for Resourcesat sensors can account for atmospheric variation within each scene and yield a surface reflectance product of higher accuracy. The visual and histograms analysis of the images before and after the correction shows that the image corrected by 6S model increased the spectral difference between ground targets and obtained wider distribution of reflectance carrying more information. The results of validation with multi date ground and contemporaneous satellite measurements show a good correlation with retrieved surface reflectance products. The impact of atmospheric correction of the quantitative retrieval of information from remote sensing images is illustrated using NDVI image as an example.

The band width of the OLI sensor is slightly different to that of RS-2 sensor especially for the NIR bands. This amounts to greater differences in the reflectance measurements in the NIR band. If NIR reflectance exceeds 40%, greater deviations are observed in the NIR and SWIR band reflectances with respect to ground truth measurements.

Amount of correlation is more in RS-2A SR products than with Rs-2 products with respect to OLI –L8 SR products. Analysing the validation results of RS2-L3 ,2016-17 SR datasets with latest 2020 SR datasets shows that deviation is more in latest 2020 datasets than 2016-17 datasets. This also agrees with the latest Cal/Val report from CVSS/DPA/NRSC. A small amount of sensor calibration may compensate these deviations.

The accuracy of the algorithm and implementation is proved by generating the L8-OLI SR datasets from this s/w which are in excellent correlation ($R^2$> 95 %) with original SR datasets downloaded from public domain. The stability and consistency of the s/w was also tested by generating SR products of highly polluted areas over different intervals of time. SR products thus generated are matching one another within 5 % deviation

| | | | Band 2 (Green ) | | | Band 3 (Red) | | | Band 4 (NIR) | | | Band 5 (SWIR) | | |
|---|---|---|---|---|---|---|---|---|---|---|---|---|---|---|
| **Satellite/Sensor** | **Path-Row-Subscene-DOP** | **OLI L8** | **slope** | **offset** | **$R^2$** | **slope** | **offset** | **$R^2$** | **slope** | **offset** | **$R^2$** | **slope** | **offset** | **$R^2$** |
| **RS2 AWiFS** | 090-054-A-22feb2020 | 150-41&42-22feb2020 | 0.982 | 0.022 | 0.939 | 0.93 | 0.019 | 0.982 | 0.94 | 0.003 | 0.937 | 0.932 | -0.043 | 0.966 |
| | 090-054-B-22feb2020 | 150-41&42-22feb2020 | 0.954 | 0.007 | 0.992 | 0.981 | 0.003 | 0.996 | 0.966 | 0.005 | 0.974 | 0.936 | -0.043 | 0.961 |
| **RS2 LISS3** | 092-044-03mar2020 | 149-34&35-02mar2020 | 0.713 | 0.008 | 0.989 | 0.769 | -0.008 | 0.984 | 0.889 | -0.019 | 0.959 | 1.015 | -0.009 | 0.946 |
| | 090-054-22feb2020 | 150-41&42-22feb2020 | 0.853 | -0.024 | 0.924 | 0.907 | -0.022 | 0.964 | 0.923 | -0.018 | 0.945 | 0.914 | -0.031 | 0.937 |
| | 101-061-24mar2020 | 143-48&49-24mar2020 | 0.927 | -0.019 | 0.959 | 1.015 | -0.009 | 0.946 | 0.885 | 0.004 | 0.97 | 1.086 | -0.015 | 0.988 |
| | 090-052 & 53- 28may2020 | 150-41&42-28may2020 | 0.844 | -0.020 | 0.936 | 0.907 | -0.018 | 0.968 | 0.955 | -0.018 | 0.956 | 0.833 | -0.026 | 0.947 |
| | 102-060-29mar2020 | 142-48-02apr2020 | 0.861 | -0.012 | 0.915 | 0.992 | -0.003 | 0.847 | 0.937 | 0.008 | 0.97 | 1.021 | -0.006 | 0.996 |
| **RS2A AWiFS** | 093-051-C-20feb2020 | 150-41-22feb2020 | 1.053 | -0.003 | 0.985 | 1.02 | 0.002 | 0.989 | 1.025 | -0.001 | 0.975 | 1.099 | -0.002 | 0.976 |
| **RS2A LISS3** | 093-051-20feb2020 | 150-41&42-22feb2020 | 0.996 | 0.001 | 0.995 | 0.943 | 0.006 | 0.993 | 0.943 | 0.007 | 0.969 | 0.945 | 0.003 | 0.994 |
| | 092-049-15feb2020 | 149-38,39,40-15feb2020 | 1.056 | -0.017 | 0.99 | 1.03 | -0.016 | 0.994 | 0.957 | 0.001 | 0.988 | 0.908 | -0.018 | 0.974 |
| | 092-050&51-03apr2020 | 149-39,40-03apr2020 | 1.045 | -0.013 | 0.983 | 1.011 | -0.014 | 0.993 | 0.949 | 0.006 | 0.989 | 0.992 | -0.016 | 0.992 |

Table 5. Slope, offset and $R^2$ for RS2/2A with OLI-L8

# 8. Product contents

- SR in separate bands
- Quality band
- BAND_META.txt
- Jpeg snapshot

# 9. References


1. Pat S. Chavez,An improved dark-object subtraction technique for atmospheric scattering correction of multispectral data, Remote Sensing of Environment,Volume 24, Issue 3,1988,Pages 459-479.
2. Coulson, K.L., Dave, J.V., and Sekera, Z., 1960, Tables related to radiation emerging from a planetary atmosphere with Rayleigh scattering, (University of California Press)
3. Clough, S.A., Shephard, M.W., Mlawer, E.J., Delamere, J.S., Iacono, M.J., Cady-Pereira, K., Boukabara S., and Brown, P.D., 2005, Atmospheric radiative transfer modeling: a summary of the AER codes, Short Communication, J. Quant. Spectrosc. Radiat. Transfer, 91, pp. 233–244.
4. Lyapustin, A., 2005, Radiative transfer code SHARM for atmospheric and terrestrial applications, Applied Optics, 44, pp. 7764–7772
5. Evans, F., and Stephens, G.L., 1991, A new polarized atmospheric radiative ransfer model, J. Quant. Spectrosc. Radiat. Transfer, 5, pp. 413–423.
6. Vermote, E. F., Member of IEEE, Tanre', D., Deuze', J. L., Herman, M., & Morcrette, J.-J. (1997). Second simulation of the satellite signal in the solar spectrum, 6S: an overview. IEEE Transactions on Geoscience and Remote Sensing, 35,675–686
7. Kotchenova, S.Y., Vermote, E.F., Levy, R., and Lyapustin, A., 2008, Radiative transfer codes for atmospheric correction and aerosol retrieval: intercomparison study, Applied Optics, 47, pp. 2215–2226
8. Sromovsky L.A., 2005,Effects of Rayleigh-Scattering polarization on reflected intensity: a fast and accurate approximation method for atmospheres with aerosols,ICARUS, 173, pp. 284–294.
9. Mishchenko, M. I., Lacis, A. A., and Travis, L. D., 1994, Errors induced by the neglect of polarization in radiance calculations for Rayleigh-scattering atmospheres. J. Quant. Spectrosc. Radiat. Transfer, 51,pp. 1491–510.
10. Tachiri, K., 2005. Calculating NDVI for NOAA/AVHRR data after atmospheric correction for extensive images using 6S code: A case study in the Marsabit District, Kenya, ISPRS Journal of Photogrammetry & Remote Sensing, 59, pp. 103–114.
11. Song, C.; Woodcock, E.C. Monitoring forest succession with multitemporal Landsat images: Factors of uncertainty. IEEE Trans. Geosci. Remote Sens. 2003, 41, 2557 -2567

12. Vermote, E. & Roger, Jean-Claude & Franch, B. & Skakun, Sergii. (2018). LaSRC (Land Surface Reflectance Code): Overview, application and validation using MODIS, VIIRS, LANDSAT and Sentinel 2 data's. 8173-8176. 10.1109/IGARSS.2018.8517622.
13. NRSC-DPA-SDPEG-SCMPAD-CVSS-JUN-2021-TR-1851-V1.0 – Radiometric Calibration of Optical Sensors using Snow Target in Gulmarg, Kashmir
14. NRSC-DPA-SDPEG-SCMPAD-CVSS-AUG-2020-TR-1644-V1.0 - Radiometric Calibration of Optical Sensors Using Natural Target at Lanela & Bap, Rajasthan.
15. Mishra V.D., J.K Singh., K. K., Thakur N K and Kumar, M. (2009). "Assessment of different topographic corrections in the AWiFS satellite imagery of Himalayan terrain". *Journal Erath System science*, Vol118(1), pp.11-26